Draft version February 6, 2020
Typeset using LaTeX **twocolumn** style in AASTeX62



# Multi-Wavelength Approach for Detecting and Characterizing Young Quasars I: Systemic Redshifts and Proximity Zones Measurements

Anna-Christina Eilers,[1,2,*] Joseph F. Hennawi,[3,2] Roberto Decarli,[4] Frederick B. Davies,[3] Bram Venemans,[2] Fabian Walter,[2] Eduardo Bañados,[2] Xiaohui Fan,[5] Emanuele P. Farina,[6] Chiara Mazzucchelli,[7] Mladen Novak,[2] Jan-Torge Schindler,[2] Robert A. Simcoe,[1] Feige Wang,[5,*] and Jinyi Yang[5]

[1] *MIT Kavli Institute for Astrophysics and Space Research, 77 Massachusetts Ave., Cambridge, MA 02139, USA*
[2] *Max-Planck-Institute for Astronomy, Königstuhl 17, 69117 Heidelberg, Germany*
[3] *Physics Department, University of California, Santa Barbara, CA 93106-9530, USA*
[4] *INAF – Osservatorio di Astrofisica e Scienza dello Spazio di Bologna, via Gobetti 93/3, I-40129, Bologna, Italy*
[5] *Steward Observatory, University of Arizona, 933 North Cherry Avenue, Tucson, AZ 85721, USA*
[6] *Max Planck Institut für Astrophysik, Karl–Schwarzschild–Straße 1, D-85748 Garching bei München, Germany*
[7] *European Southern Observatory, Alonso de Cordova 3107, Vitacura, Region Metropolitana, Chile*

Submitted to ApJ

## ABSTRACT

In a multi-wavelength survey of 13 quasars at $5.8 \lesssim z \lesssim 6.5$, we find five objects with extremely small proximity zone sizes that may imply UV–luminous lifetimes of $\lesssim 100,000$ years. Proximity zones are regions of enhanced transmitted flux in the vicinity of the quasars that are sensitive to the quasars' lifetimes because the intergalactic gas has a finite response time to their radiation. We combine sub-mm observations from the Atacama Large Millimetre Array (ALMA) and the NOrthern Extended Millimeter Array (NOEMA), as well as deep optical and near-infrared spectra from medium-resolution spectrographs on the Very Large Telescope (VLT) and on the Keck telescopes, in order to identify and characterize these new young quasars, which provide valuable clues about the accretion behavior of supermassive black holes (SMBHs) in the early universe, and pose challenges on current black hole formation models to explain the rapid formation of billion solar mass black holes. We measure the quasars' systemic redshifts, black hole masses, Eddington ratios, emission line luminosities, and star formation rates of their host galaxies. Combined with previous results we estimate the fraction of young objects within the high–redshift quasar population at large to be $5\% \lesssim f_{\rm young} \lesssim 9\%$. One of these objects, PSO J158–14, shows one of the brightest [C II] emission lines ($F_{\rm line} = 7.18 \pm 0.33$ mJy) observed to date in high–redshift quasars, and thus indicates a highly star–bursting host galaxy with a star formation rate of approximately $1200\,M_\odot\,{\rm yr}^{-1}$.

*Keywords:* dark ages, early universe — quasars: emission lines, supermassive black holes — methods: data analysis — intergalactic medium — submillimeter: ISM, galaxies

## 1. INTRODUCTION

High-redshift quasars host central supermassive black holes (SMBHs) with masses exceeding $M_{\rm BH} \sim 10^9 - 10^{10}\ M_\odot$ as early as $\lesssim 1$ Gyr after the Big Bang (e.g. Mortlock et al. 2011; Venemans et al. 2013; Wu et al. 2015; Mazzucchelli et al. 2017; Bañados et al. 2018; Onoue et al. 2019). How these SMBHs form and grow in such short amounts of cosmic time remains an unanswered question. Assuming Eddington limited accretion rates and a constant supply of fueling material SMBHs grow exponentially during the quasar's lifetime $t_{\rm Q}$, i.e.

$$M_{\rm BH}(t_{\rm Q}) = M_{\rm seed} \cdot \exp\left(\frac{t_{\rm Q}}{t_{\rm S}}\right). \quad (1)$$

The initial mass $M_{\rm seed}$ denotes the mass of the black hole before the onset of quasar activity. The lifetime or the age of a quasar $t_{\rm Q}$ is defined such that the onset

Corresponding author: Anna-Christina Eilers
eilers@mit.edu

* NASA Hubble Fellow

of the quasar activity happened at a time $-t_{\rm Q}$ in the past. The e-folding time, or "Salpeter" time, $t_{\rm S}$ (Salpeter 1964), describes the characteristic time scale on which the black hole growth is believed to occur, i.e.

$$t_{\rm S} = 4.5 \times 10^7 \left(\frac{\epsilon}{0.1}\right) \left(\frac{L}{L_{\rm Edd}}\right) \text{ yr}, \quad (2)$$

where $\epsilon$ denotes the radiative efficiency of the accretion, which is assumed to be about 10% in thin accretion disk models (Shakura & Sunyaev 1973), and $L$ describes the bolometric luminosity of the quasar with a theoretical upper limit of the Eddington luminosity $L_{\rm Edd}$. It requires at least 16 e-foldings, i.e. $\gtrsim 7 \times 10^8$ yr, in order to grow a billion solar mass black hole from an initial stellar remnant black hole seed with $M_{\rm seed} \sim 100\,M_{\odot}$, even if they accrete continuously at the Eddington limit (e.g. Volonteri 2010, 2012). However, it is currently unknown whether quasars obey this exponential light curve, or if other physics related to the triggering of quasar activity and the supply of fuel complicate this simple picture, giving rise to much more complex light curves (e.g. Di Matteo et al. 2005; Springel et al. 2005; Hopkins et al. 2005; Novak et al. 2011; Davies et al. 2019b).

These timescales required for the growth of SMBHs are comparable to the age of the universe at $z \gtrsim 6$. Nevertheless, at these high redshifts more than 200 quasars have been discovered in the last decade (e.g. Venemans et al. 2015; Bañados et al. 2016; Mazzucchelli et al. 2017; Wang et al. 2019; Yang et al. 2019a; Reed et al. 2019), many of which host billion solar mass black holes. Thus, massive initial seeds in excess of stellar remnants, i.e. $M_{\rm seed} \gtrsim 1000\,M_{\odot}$ (e.g. Lodato & Natarajan 2006; Visbal et al. 2014; Habouzit et al. 2016; Schauer et al. 2017), or radiatively inefficient accretion rates with $\epsilon \lesssim 0.01 - 0.001$ have been invoked (e.g. Volonteri et al. 2015; Trakhtenbrot et al. 2017; Davies et al. 2019a), which would reduce the quasar lifetime required to grow the SMBHs.

Measurements of quasar lifetimes have proven to be challenging. At low redshifts, i.e. $z \sim 2 - 4$, the quasar lifetime can be constrained by comparing the number density of quasars to their host dark matter halo abundance inferred from clustering studies (Haiman & Hui 2001; Martini & Weinberg 2001; Martini 2004; White et al. 2008). However, to date this method has yielded only weak constraints on $t_{\rm Q} \sim 10^6 - 10^9$ yr owing to uncertainties in how quasars populate dark matter halos (Shen et al. 2009; White et al. 2012; Conroy & White 2013; Cen & Safarzadeh 2015). Following the "Soltan" argument (Soltan 1982), which states that the luminosity function of quasars as a function of redshift reflects the gas accretion history of local remnant black holes, Yu & Tremaine (2002) estimated the mean lifetime of luminous quasars from local early-type galaxies to be $t_{\rm Q} \sim 10^7 - 10^8$ yr. Further constraints on quasar activity on timescales between $\sim 10^5 - 10^7$ yr have been set by measuring an ionization "echo" of the quasar, which denotes the time-lag between changes in the quasar's ionization rate and the responding changes in the opacity of the surrounding IGM (Adelberger 2004; Hennawi et al. 2006; Schmidt et al. 2017; Bosman et al. 2019). A recent compilation of studies on the timescales governing the growth of SMBHs can be found in Inayoshi et al. (2019).

We recently showed how the extent of the proximity zones around high-redshift quasars provides a new and independent constraint on the lifetime of quasars (Eilers et al. 2017a; Khrykin et al. 2019; Davies et al. 2019a). These regions of enhanced transmitted flux within the Ly$\alpha$ forest in the immediate vicinity of the quasars have been ionized by the quasar's intense radiation itself (e.g. Bajtlik et al. 1988; Haiman & Cen 2001; Wyithe et al. 2005; Bolton & Haehnelt 2007a; Lidz et al. 2007; Bolton et al. 2011; Keating et al. 2015), and are sensitive to the lifetime of the quasars because intergalactic gas has a finite response time to the quasars' radiation (e.g. Khrykin et al. 2016; Eilers et al. 2017a; Davies et al. 2019b). The equilibration timescale $t_{\rm eq}$ describes the time when the intergalactic medium (IGM) has reached ionization equilibrium with the ionizing photons emitted by the quasar, i.e. $t_{\rm eq} \approx \Gamma_{\rm HI}^{-1}$, where $\Gamma_{\rm HI}$ denotes the total photoionization rate from the quasar as well as the ultraviolet background (UVB). However, the quasar's radiation dominates the radiation field within the proximity zone, which has been observationally defined as the location at which the smoothed, continuum-normalized transmitted flux drops below the 10%-level (Fan et al. 2006). A photoionization rate of $\Gamma_{\rm HI} \approx 10^{-12}\,{\rm s}^{-1}$ from the quasar's radiation at the "edge" of the proximity zone at $z \approx 6$ leads to an equilibration timescale of $t_{\rm eq} \approx 3 \times 10^4$ yr (Davies et al. 2019b).

Applying this new method to a data set of 34 quasar spectra at $5.8 \lesssim z \lesssim 6.5$ (Eilers et al. 2018a), we discovered an unexpected population of quasars with significantly smaller proximity zones than expected, that are likely to be very young, i.e. $t_{\rm Q} \lesssim 10^4 - 10^5$ yr (Eilers et al. 2017a, 2018b). These young quasars provide valuable clues to the accretion behavior of SMBHs, and pose significant challenges on current black hole formation models that require much longer lifetimes to explain the growth of SMBHs.

This study aims to determine the fraction of such young objects within the quasar population at large, and to establish a statistically uniform and significant

sample of young quasars, which will then enable us to search for any spectral or environmental signatures that might distinguish these young objects from the whole quasar population. To this end, we conduct preliminary measurements of the proximity zones $R_p$ of approximately 120 quasars at $5.6 \lesssim z \lesssim 6.5$. However, these preliminary measurements have large uncertainties, i.e. $\Delta R_p \sim 1.5$ pMpc, mostly due to their imprecise redshift estimates, i.e. $\Delta v \sim 1000\,\mathrm{km\,s^{-1}}$, which are based on broad rest-frame UV emission lines that can be displaced from the systemic redshift due to strong internal motions or winds. These uncertainties on the redshift estimates constitute the largest source of uncertainty in the measurements of proximity zones. We select 13 young quasar "candidates", which have been chosen because the preliminary measurements of their proximity zones were very small, and thus they potentially indicate very short quasar lifetimes. For these young candidates we conduct a multi-wavelength survey, in order to obtain precise measurements of the quasars' systemic redshifts and to estimate the quasar lifetimes based on the extents of their proximity zones.

We measure the systemic redshifts by means of sub-mm emission lines arising from the cold gas reservoir of the quasar host galaxies with the Atacama Large Millimetre Array (ALMA) and the NOrthern Extended Millimeter Array (NOEMA) at the Institute de Radioastronomie Millimétrique (IRAM). These emission lines provide a tenfold improvement on the quasars' systemic redshifts, because they do not suffer from possible displacements due to strong internal motions or winds in the quasars' broad line regions (BLR). Furthermore, we obtained deep optical and near-infrared (NIR) spectra with the medium resolution spectrographs X-Shooter on the Very Large Telescope (VLT) and the Deep Imaging Multi-Object Spectrograph (DEIMOS) on the Keck telescopes to search for associated absorption systems that might have contaminated and prematurely truncated the quasars' proximity zones.

In this paper we present the multi-wavelength data of our study, measure precise systemic redshifts and update the quasars' proximity zone measurements. In a following paper (Eilers et al. in prep., hereafter Paper II) we will use these measurements to derive constraints on the quasars' lifetimes, and study the dependence of spectral properties with quasar age.

Throughout this paper, we assume a flat ΛCDM cosmology of $h = 0.677$, $\Omega_m = 0.307$, and $\Omega_\Lambda = 0.691$ (Planck Collaboration et al. 2014).

## 2. QUASAR SAMPLE

We target quasars that are likely to have short lifetimes, as indicated by a very small proximity zone. To this end we analyzed the spectra of $\approx 120$ quasars at $5.6 \lesssim z \lesssim 6.5$. These spectra were taken with a variety of different telescopes and instruments, and thus cover different wavelength ranges, have different spectral resolutions, and different signal-to-noise ratios (see Willott et al. 2009; Bañados et al. 2016; Reed et al. 2017; Wang et al. 2017; Farina et al. 2019, for details). Based on these spectra we conducted preliminary estimates of the quasars' proximity zone sizes (see § 4.3 and § 4.4 for details on the procedure for measuring proximity zones). However, these measurements have large uncertainties due to the highly uncertain redshift estimates (up to $\Delta v \sim 1000\,\mathrm{km\,s^{-1}}$), which were based on template fitting or the Ly$\alpha$ emission line.

Since brighter quasars emit more ionizing radiation and thus have a larger proximity zone size for a given age, we normalized the preliminary proximity zone estimates to the same absolute magnitude of $M_{1450} = -27$, in order to eliminate the dependence of the proximity zone sizes on the quasars' luminosities. These "corrected" proximity zones $R_{p,\,\mathrm{corr}}$ of our sample span a range of 0.6 pMpc $\lesssim R_{p,\,\mathrm{corr}} \lesssim$ 12.1 pMpc, with a mean of $\langle R_{p,\,\mathrm{corr}} \rangle \approx 5.4$ pMpc.

We choose 13 objects with very small preliminary proximity zone estimates, i.e. $R_{p,\,\mathrm{corr}} \lesssim 2$ pMpc, for follow–up multi–wavelength observations. We aim to exclude any objects that showed evidence for a premature truncation of the proximity zones due to associated absorption systems, such as proximate damped Ly$\alpha$ absorption systems (pDLAs), which we identify by searching for ionic metal absorption lines in the quasar continuum that are associated with the absorber. Such quasars with associated absorption systems spuriously resemble quasars with small proximity zones. Additionally, we exclude quasars with broad absorption lines (BALs) that might contaminate the proximity zones. Based on these criteria we select the $\sim 10\%$ of quasars with the smallest proximity zone measurements.

One object in this sample, CFHQS J2229+1457, was previously identified to have a small proximity zone, but the available spectrum obtained with the Low Resolution Imaging Spectrometer (LRIS) on Keck did not have sufficient resolution to securely exclude any premature truncation of its proximity zone (Eilers et al. 2017a). The complete quasar sample of this study is listed in Table 1.

## 3. MULTI-WAVELENGTH DATA SET

We present a multi-wavelength data set, including sub-mm data acquired from ALMA (§ 3.1) and

**Table 1.** Overview of our data set sorted by right ascension.

| object | RA [hms] | DEC [dms] | instrument | $t_{\rm exp}$ [hr] | program ID |
|---|---|---|---|---|---|
| PSO J004+17 | 00:17:34.467 | +17:05:10.696 | ALMA | 0.6 | 2017.1.00332.S (PI: Eilers) |
| | | | VLT/X-Shooter | 1.0 | 101.B-02720 (PI: Eilers) |
| PSO J011+09 | 00:45:33.566 | +09:01:56.928 | ALMA | 0.3 | 2017.1.00332.S (PI: Eilers) |
| | | | VLT/X-Shooter | 1.0 | 101.B-02720 (PI: Eilers) |
| VDES J0323–4701 | 03:23:40.340 | –47:11:29.400 | VLT/X-Shooter | 0.7 | 101.B-02720 (PI: Eilers) |
| VDES J0330–4025 | 03:30:27.920 | –40:25:16.200 | VLT/X-Shooter | 0.7 | 101.B-02720 (PI: Eilers) |
| PSO J056–16 | 03:46:52.044 | –16:28:36.876 | ALMA | 0.3 | 2017.1.00332.S (PI: Eilers) |
| | | | X-Shooter | 2.0 | 097.B-1070 (PI: Farina) |
| PSO J158–14 | 10:34:46.509 | –14:25:15.855 | ALMA | 0.3 | 2017.1.00332.S (PI: Eilers) |
| | | | VLT/X-Shooter | 1.2 | 096.A-0418 (PI: Shanks) |
| SDSS 1143+3808 | 11:43:38.347 | +38:08:28.823 | IRAM/NOEMA | 4.0 | W18EF (PI: Eilers) |
| | | | Keck/DEIMOS | 1.0 | 2017A_U078 (PI: Hennawi) |
| PSO J239–07 | 15:58:50.990 | –07:24:09.591 | ALMA | 0.4 | 2017.1.00332.S (PI: Eilers) |
| | | | VLT/X-Shooter | 1.0 | 101.B-02720 (PI: Eilers) |
| PSO J261+19 | 17:24:08.746 | +19:01:43.120 | IRAM/NOEMA | 2.5 | W18EF (PI: Eilers) |
| | | | VLT/X-Shooter | 1.0 | 101.B-02720 (PI: Eilers) |
| PSO J265+41 | 17:43:43.136 | +41:24:50.191 | IRAM/NOEMA | 2.5 | W18EF (PI: Eilers) |
| | | | Keck/DEIMOS | 1.0 | 2017B_U090 (PI: Hennawi) |
| CFHQS J2100–1715 | 21:00:54.616 | –17:15:22.500 | VLT/X-Shooter | 3.3 | 097.B-1070 (PI: Farina) |
| CFHQS J2229+1457 | 22:29:01.649 | +14:57:08.980 | VLT/X-Shooter | 1.7 | 101.B-02720 (PI: Eilers) |
| PSO J359-06 | 23:56:32.451 | –06:22:59.255 | ALMA | 0.3 | 2017.1.00332.S (PI: Eilers) |
| | | | VLT/X-Shooter | 1.3 | 098.B-0537 (PI: Farina) |

Note—The columns show the name of the quasar, its coordinates RA and DEC in the J2000 epoch, as well as the instrument with which the data was taken, the exposure time on the source, and the program ID of the observation.

NOEMA, (§ 3.2), as well as optical/NIR data obtained with VLT/X-Shooter (§ 3.3), and optical data observed with the Keck/DEIMOS (§ 3.4). Table 1 shows a summary of the observations presented in this paper.

### 3.1. *ALMA Observations*

The ALMA data consist of short ($\sim 15-20$ minutes on source) observations centered on the optical/NIR coordinates of the quasars. The tuning frequency of the spectral windows was chosen such that two neighbouring windows encompass the expected observed frequency of the [C II] emission line at 158 $\mu$m ($\nu_{\rm rest} = 1900.548$ GHz) based on preliminary redshift estimates. The other two spectral windows cover the dust continuum emission. Observations were carried out in May 2018 with the array in a compact configuration C43 – 2, resulting in images with $\sim 1''$ spatial resolution. Thus, the size of the [C II]-emitting region is comparable to the expected sizes of the quasar host galaxies and hence the sources are likely unresolved (Walter et al. 2009).

The data were processed with the default calibration procedure making use of the CASA pipeline (McMullin et al. 2007), version 5.1.2. The data cubes were then imaged with the CASA command `tclean` using Briggs cleaning and a robust parameter of 2 (natural weighting), in order to maximize the signal-to-noise ratio (SNR) of our observations. The mean rms noise is 0.34 mJy beam$^{-1}$ per 30 MHz bin.

We calculate the continuum flux $F_{\rm cont}$ making use of the extracted 1D spectrum from the remaining two line-free spectral windows. The pure line map is obtained by subtracting the continuum emission applying the CASA command `uvcontsub`, and afterwards collapsing the data cube within a narrow frequency range ($\Delta\nu = 0.4$ GHz for PSO J158–14 due to its broad [C II] line, and $\Delta\nu = 0.25$ GHz for all other objects) around the peak frequency of the emission line. All images of the collapsed and continuum-subtracted line maps are shown in the top six panels in Fig. 1. The dust continuum maps are shown in Appendix C in Fig. 8.

### 3.2. *NOEMA Observations*

Three quasars from our sample located in the Northern hemisphere have been observed with the ten anten-

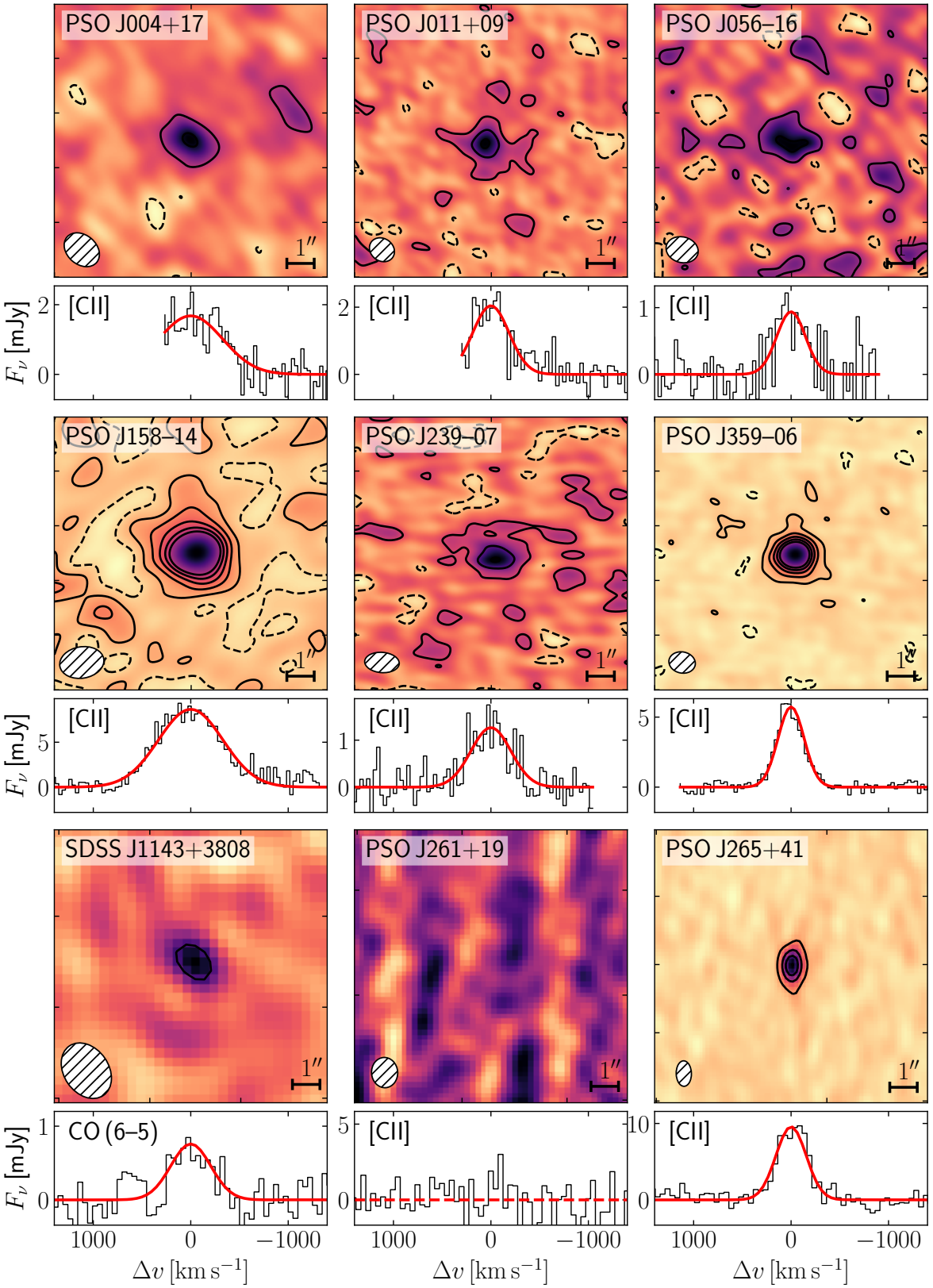


**Figure 1. [C II] and CO emission line maps.** The six quasars in the top 2 rows show observations with ALMA, while the bottom row shows three quasars that have been observed with NOEMA. The upper panels of each source present the collapsed and continuum-subtracted line maps ($10'' \times 10''$ in size), where the black solid and dashed contours indicate the $\pm 1, 3, 5, 7, 9\sigma$ isophotes. The bottom panels show the extracted spectra (black) at the brightest peak position, as well as the best Gaussian fit (red) to their emission line.

nas of NOEMA in compact configuration (10C) in December 2018 and January 2019. Taking advantage of the PolyFix correlator we could simultaneously collect data in an upper and lower side band with a total band width of 15.4 GHz. The data were calibrated and reduced making use of the `GILDAS` routine `clic`.

The visibilities were imaged using the software `mapping` as part of the `GILDAS` suite. We adopt natural weighting, which results in a synthesized beam size of $0.5'' \times 0.9''$ at the higher tuning frequency $\nu_{\rm obs} = 270.49$ GHz for PSO J265+41, and $1.6'' \times 2.2''$ at a lower tuning frequency of $\nu_{\rm obs} = 101.14$ GHz for SDSS J1143+3808, for which we observed the CO(6–5) at 3 mm ($\nu_{\rm rest} = 691.473$ GHz) and CO(5–4) ($\nu_{\rm rest} = 576.267$ GHz) emission lines instead of [C II]. The imaged cubes are re-binned on a spectral axis with $50\,{\rm km\,s^{-1}}$ wide channels. The rms noise for SDSS J1143+3808 is $0.21\,{\rm mJy\,beam^{-1}}$ per $50\,{\rm km\,s^{-1}}$ bin, whereas the other two observations for PSO J261+19 and PSO J265+41 have a larger rms noise of $1.18\,{\rm mJy\,beam^{-1}}$ and $1.01\,{\rm mJy\,beam^{-1}}$ per $50\,{\rm km\,s^{-1}}$ bin, respectively. The continuum flux is estimated from the extracted 1D spectrum using the line-free channels, and subtracted from the cubes. The bottom three panels of Fig. 1 show the continuum subtracted line maps obtained with NOEMA.

### 3.3. *VLT/X-Shooter Observations*

Most quasar spectra observed with X-Shooter on the VLT were obtained on August 18th and 19th, 2018, in visitor mode (program ID: 101.B-02720). The data of four quasar spectra, i.e. PSO J056–16, PSO J158–14, CFHQS J2100–1715, and PSO J359–06 were acquired between January 2016 and May 2017, and are taken from the ESO archive[1] (Chehade et al. 2018, Farina et al. in prep.). We obtained multiple exposures of 1200 s each, with the $0.6'' \times 11''$ slit in the NIR, and the $0.9'' \times 11''$ slit in the VIS. The VIS observations are binned $2 \times 2$ in spectral and spatial direction. Using a $0.9''$ slit width we obtain a spectral resolution of $R \approx 8900$ in the visible wavelength regime and $R \approx 8100$ in the NIR arm for a $0.6''$ slit[2]. The wavelength range covers $5500\text{Å} \lesssim \lambda_{\rm obs} \lesssim 22000\text{Å}$. We dithered the different exposures along the slit to allow for image differencing in the data reduction step (see § 3.4). One object, PSO J158–14, has been observed with the wider $0.9''$ slit in the NIR ($R \approx 5600$) and the $K$-band blocking filter, which results in a reduced wavelength coverage of $5500\text{Å} \lesssim \lambda_{\rm obs} \lesssim 20250\text{Å}$.

### 3.4. *Keck/DEIMOS Observations*

The two quasar spectra taken with the DEIMOS instrument at the Nasmyth focus on the Keck II telescope were observed in May and September 2017. For each object we acquired three exposures of 1200 s each. In the case of SDSS J1143+3808 we used a custom-made slitmask with a $1''$ slit and the 830G grating, resulting in a pixel scale of $\Delta\lambda \approx 0.47$ Å and a spectral resolution of $R \approx 2500$. For PSO J265+41 we used the same grating, but the `LongMirr` slitmask with a narrower ($0.7''$) slit, resulting in a slightly higher resolution. The grating was tilted to a central wavelength of 8400 Å, resulting in a wavelength coverage of $6530\text{Å} \lesssim \lambda_{\rm obs} \lesssim 10350\text{Å}$.

All optical and NIR spectroscopic data were reduced applying standard data reduction techniques with the newly developed open source python spectroscopic data reduction package `PypeIt`[3] (Prochaska et al. 2019). The reduction procedure includes sky subtraction, which was performed on the 2D images by including both image differencing between dithered exposures (whenever these were available) and a B-spline fitting procedure. In order to then extract the 1D spectra the optimal spectrum extraction technique is applied (Horne 1986). The individual 1D spectra are flux calibrated using the standard stars LTT 3218 (for spectra observed with VLT/X-Shooter) and G191B2B or Feige 110 (for spectra taken with Keck/DEIMOS). Finally, the fluxed 1D spectra are stacked and a telluric model is fitted to the stacked spectra using telluric model grids produced from the Line-By-Line Radiative Transfer Model (LBLRTM[4]; Clough et al. 2005; Gullikson et al. 2014), resulting in the final spectra.

Fig. 2 and Fig. 3 show the final reduced optical and NIR spectra for all quasars in our sample. We apply a running 20 pixel filter when showing the spectra and noise vectors with the average flux computed using inverse variance weights.

## 4. ANALYSIS

In this section we analyze our multi-wavelength data set to measure the quasars' systemic redshifts (§ 4.1 and § 4.2), and estimate their optical continuum emission (§ 4.3), in order to measure the extents of their proximity zones (§ 4.4). We determine further properties of the quasars, such as the star formation rates (SFR) of the

[1] http://archive.eso.org/eso/eso_archive_main.html

[2] https://www.eso.org/sci/facilities/paranal/instruments/xshooter/inst.html

[3] DOI: 10.5281/zenodo.3506873

[4] http://rtweb.aer.com/lblrtm.html

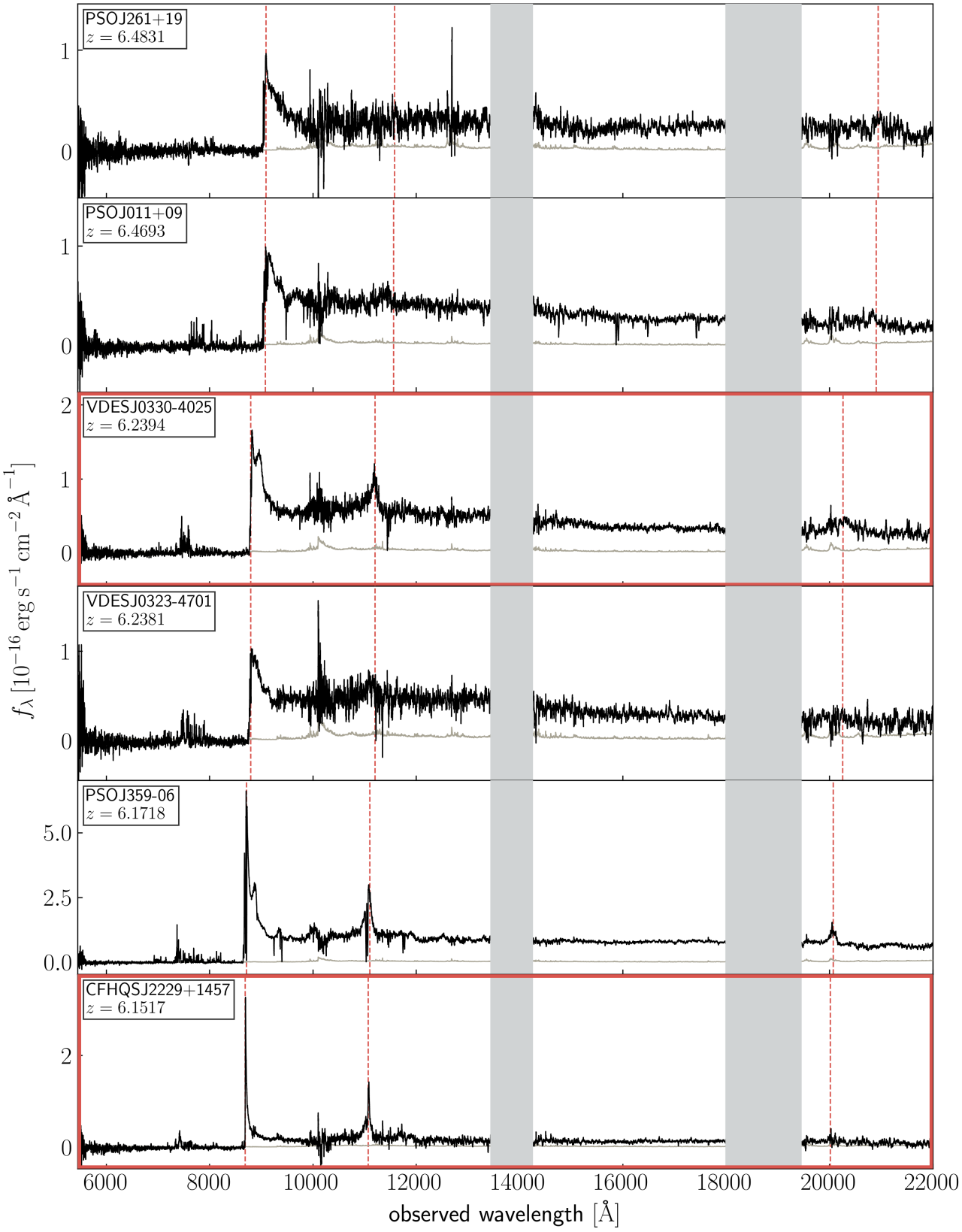


**Figure 2. Spectra of the quasars in our sample.** All spectra (black) are observed with VLT/X-Shooter, besides the spectra of the two quasars PSO J265+41 and SDSS J1143+3808, which have been observed with Keck/DEIMOS. Regions of large telluric absorption have been masked with grey shaded regions. The dashed red lines indicate the location of various emission lines, i.e. Ly$\alpha$ at 1215.7 Å in the rest-frame, the C IV doublet at 1548 Å and 1550 Å, as well as the Mg II emission line at 2798.7 Å. All spectra and noise vectors (grey) have been inverse-variance smoothed with a 20 pixel filter. The red frames indicate quasars that exhibit very small proximity zones, i.e. $R_{p,\,\mathrm{corr}} \lesssim 2$ pMpc.

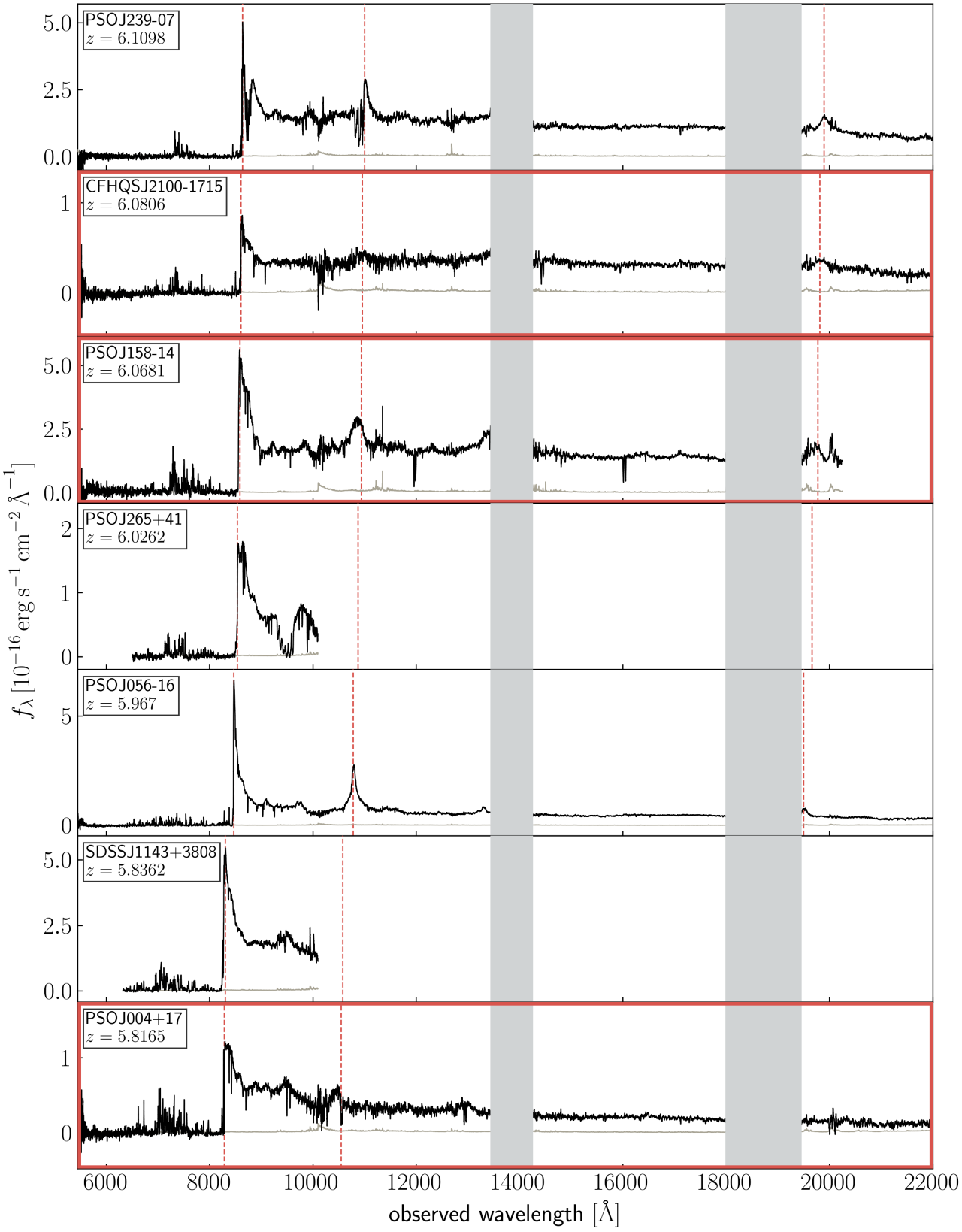


**Figure 3.** Same as Fig 2.

host galaxies (§ 4.5), as well as the black hole masses and the Eddington ratios of the accretion.

### 4.1. *Systemic Redshifts of Quasar Host Galaxies*

The most precise estimates of the systemic redshifts of quasars are based on the narrow atomic or molecular emission lines arising from the gas reservoir within the quasars' host galaxy. We estimate the systemic redshifts primarily by means of the [C II] emission line, which is the dominant coolant of the ISM. For one quasar in our sample, SDSS J1143+3803, this line was outside of the observable frequency range of NOEMA, and thus we observed the CO(6–5) and CO(5–4) emission lines, which usually are some of the brightest molecular CO transitions in quasars (e.g. Carilli & Walter 2013; Yang et al. 2019b). Because these lines arise from the host galaxy itself, they provide a much more precise redshift estimate compared to rest-frame UV emission lines that arise from the BLR around quasars and may suffer from strong internal motions or winds, potentially displacing the emission line centers from the systemic redshift (e.g. Richards et al. 2002; Venemans et al. 2016; Mazzucchelli et al. 2017).

We extract the 1D spectra from the continuum-subtracted data cubes at the position of the brightest emission from the source. We then fit the [C II] or CO emission lines assuming a Gaussian line shape. We apply the Markov Chain Monte Carlo (MCMC) affine-invariant ensemble sampler `emcee` (Foreman-Mackey et al. 2013) with flat priors for the amplitude $A \in [0, 20]$ mJy, the width $\sigma \in [0, 1]$ GHz of the emission line, as well as the peak frequency $\nu_{\rm obs}$. We adopt the median of the resulting posterior probability distribution as the best parameter estimate. We take the peak of the Gaussian fit as the best estimate for the systemic redshift of the quasar with an uncertainty arising from the 68th percentile of the posterior probability distribution.

The extracted spectra and the corresponding best fit to the sub-mm emission lines are shown in the lower panels of each object in Fig. 1. Table 2 shows the estimated parameters derived from the sub-mm emission lines of the quasars. Note that in one case (PSO J261+19) no clear detection of an emission line associated with the quasar host galaxy could be found, and we extracted the spectrum at the nominal position of the target based on optical/NIR data. Since we also do not detect any continuum emission from this source (see Fig. 8 in Appendix A), this non-detection is likely explained by a very faint emission that is below the detection limit of our 2.5 hour exposure with NOEMA, i.e. $F_{\rm cont} < 0.15$ mJy, rather than by a wrong redshift estimate that might have shifted the emission line outside of the detectable frequency range.

### 4.2. *Mg II Redshifts, Black Hole Masses, and Eddington Ratios*

For the subset of quasars for which we did not obtain a sub-mm redshift measurement (VDES J323-4701, VDES J0330-4025, and PSO J261+19), we estimate their redshift by means of the Mg II emission line at $\lambda$2798.7 Å observable in the NIR spectra. The Mg II emission arises within the BLR of the quasars and may suffer from velocity shifts with respect to the systemic redshift. However, for the majority of quasars we only expect modest velocity shifts (Richards et al. 2002; Venemans et al. 2016; Mazzucchelli et al. 2017), and thus calculate a redshift estimate $z_{\rm Mg\,II}$ from the peak of the line. To this end, we model the quasar emission within the wavelength region around the Mg II emission line, i.e. 2100 Å$\leq \lambda_{\rm rest} \leq$ 3089 Å, as a superposition of a power-law continuum with a slope $\alpha$ arising from the quasar's accretion disk, a scaled template spectrum of the iron lines Fe II and Fe III, $f_{\lambda,\,\rm iron}$, within the BLR, as well as a single Gaussian to model the Mg II emission line, i.e.

$$f_\lambda = a_0 \cdot \lambda^{-\alpha} + a_1 \cdot f_{\lambda,\,\rm iron} + a_2 \cdot \exp\left(-\frac{(\lambda - \mu_{\rm MgII})^2}{2\sigma^2_{\rm MgII}}\right),$$

where $a_0$, $a_1$, and $a_2$ denote the amplitudes of the individual components. We apply the iron template spectrum from Vestergaard & Wilkes (2001), which has been derived from a narrow emission line quasar, and convolve it with a Gaussian kernel with FWHM $\approx$ FWHM$_{\rm Mg\,II}$ to mimic the quasars' broad emission lines.

We estimate the free parameters of the fit by means of the MCMC sampler `emcee`, assuming again flat priors and adopting the median of the posterior probability distribution as our best estimate. From the peak of the Mg II emission line we can then derive the redshift estimate $z_{\rm MgII}$. All fits to the Mg II emission lines are shown in Fig. 9 in Appendix B.

The luminosity $L_{\lambda,\,3000\text{Å}}$ as well as the full width at half maximum (FWHM) of the Mg II line obtained from the single-epoch NIR spectra of 10 of the quasars in our sample allows us to estimate the mass of the central SMBH, under the assumption that the dynamics in the quasar's BLR are dominated by the gravitational pull of the black hole and thus the virial theorem can be applied. We estimate the mass of the black hole by means of the scaling relation

$$\frac{M_{\rm BH}}{M_\odot} = 10^{6.86}\left(\frac{\rm FWHM_{MgII}}{10^3\,{\rm km\,s^{-1}}}\right)^2\left(\frac{\lambda L_{\lambda,\,3000\text{Å}}}{10^{44}\,{\rm erg\,s^{-1}}}\right)^{0.5},$$

which has been calibrated using scaling relations from other emission lines with several thousand quasar spec-

**Table 2.** Measurements of sub-mm properties of the quasar sample.

| object | line | $\nu_{\rm obs}$ [GHz] | $z_{\rm sys}$ | FWHM [km s$^{-1}$] | $F_{\rm cont}$ [mJy] | $F_{\rm line}$ [Jy km s$^{-1}$] | $\log L_{\rm line}$ [L$_\odot$] |
|---|---|---|---|---|---|---|---|
| PSO J004+17 | [C II] | $278.82 \pm 0.04$ | $5.8165 \pm 0.0004$ | $770 \pm 96$ | $0.74 \pm 0.05$ | $1.38 \pm 0.20$ | $9.11 \pm 0.07$ |
| PSO J011+09 | [C II] | $254.45 \pm 0.02$ | $6.4693 \pm 0.0002$ | $439 \pm 79$ | $0.82 \pm 0.04$ | $0.96 \pm 0.21$ | $9.02 \pm 0.09$ |
| PSO J056–16 | [C II] | $272.79 \pm 0.03$ | $5.9670 \pm 0.0003$ | $347 \pm 69$ | $0.11 \pm 0.03$ | $0.35 \pm 0.09$ | $8.53 \pm 0.12$ |
| PSO J158–14 | [C II] | $268.89 \pm 0.01$ | $6.0681 \pm 0.0001$ | $779 \pm 28$ | $2.92 \pm 0.04$ | $7.18 \pm 0.33$ | $9.86 \pm 0.02$ |
| SDSS J1143+3808 | CO(6–5) | $101.14 \pm 0.02$ | $5.8367 \pm 0.0010$ | $438 \pm 109$ | $0.07 \pm 0.01$ | $0.32 \pm 0.11$ | $8.04 \pm 0.18$ |
| | CO(5–4) | $84.30 \pm 0.01$ | $5.8355 \pm 0.0005$ | $362 \pm 61$ | $0.05 \pm 0.01$ | $0.25 \pm 0.05$ | $7.86 \pm 0.09$ |
| PSO J239–07 | [C II] | $267.32 \pm 0.02$ | $6.1098 \pm 0.0002$ | $484 \pm 60$ | $0.17 \pm 0.03$ | $0.65 \pm 0.11$ | $8.82 \pm 0.07$ |
| PSO J261+19 | [C II] | – | – | – | $< 0.15$ | – | – |
| PSO J265+41 | [C II] | $270.50 \pm 0.02$ | $6.0262 \pm 0.0002$ | $365 \pm 57$ | $3.13 \pm 0.10$ | $3.72 \pm 0.78$ | $9.57 \pm 0.08$ |
| CFHQS J2100–1715 | [C II] | $268.39 \pm 0.02^b$ | $6.0806 \pm 0.0011^a$ | $340 \pm 70^a$ | $1.20 \pm 0.15^a$ | $1.37 \pm 0.14^a$ | $9.12 \pm 0.04^a$ |
| CFHQS J2229+1457 | [C II] | $265.75 \pm 0.02^c$ | $6.1517 \pm 0.0005^c$ | $351 \pm 39^c$ | $0.05 \pm 0.03^c$ | $0.58 \pm 0.08^c$ | $8.78 \pm 0.06^c$ |
| PSO J359–06 | [C II] | $265.0 \pm 0.01$ | $6.1718 \pm 0.0001$ | $318 \pm 14$ | $0.49 \pm 0.03$ | $1.93 \pm 0.12$ | $9.30 \pm 0.03$ |

Note—The columns show the name of the quasar, the observed sub-mm emission line, its peak frequency, the derived systemic redshift, the FWHM of the observed line, the continuum and integrated line fluxes, and the line luminosity. Parameters for CFHQS J2100–1715 are derived by (*a*) Decarli et al. (2017), and (*b*) Decarli et al. (2018), while parameters for CFHQS J2229+1457 are taken from (*c*) Willott et al. (2015).

tra from the Sloan Digital Sky Survey (SDSS; Vestergaard & Osmer 2009). This scaling relation has an intrinsic scatter of approximately 0.55 dex.

Knowing the black hole masses we can derive the Eddington luminosity $L_{\rm Edd}$ of the quasars, as well as the Eddington ratio of their accretion, i.e. $\lambda_{\rm Edd} = L_{\rm bol}/L_{\rm Edd}$. All measurements of the NIR properties are shown in Table 3.

### 4.3. *Quasar Continuum Estimates*

Measurements of proximity zone sizes require a prediction for the underlying quasar continua. We estimate the quasar continua by means of a principal component analysis (PCA) that decomposes a set of training spectra into an orthogonal basis (Suzuki et al. 2005; Pâris et al. 2011; Davies et al. 2018). Following Davies et al. (2018), we construct a PCA decomposition based on 12,764 training spectra from the SDSS BOSS sample in the logarithmic flux space, such that each quasar spectrum $f_\lambda$ can be approximated via

$$\log f_\lambda \approx \langle \log f_\lambda \rangle + \sum_{i=0}^{N_{\rm PCA}} a_i A_i, \tag{3}$$

where $\langle \log f_\lambda \rangle$ is the mean logarithmic flux and $A_i$ are the PCA components, weighted by the coefficients $a_i$. The logarithmic space has been chosen, because variations of the power-law quasar continuum are more naturally described by a multiplicative component rather than additive components (e.g. Lee et al. 2012).

Because quasar spectra at high redshifts suffer from significant absorption bluewards of the Ly$\alpha$ emission line due to residual neutral hydrogen in the IGM, we follow the approach of previous work (Suzuki et al. 2005; Pâris et al. 2011), and estimate the PCA coefficients only on the red side of the spectra. To this end, we construct a set 10 "red" PCA components $R_i$ between 1220 Å $\leq \lambda_{\rm rest} \leq$ 2850 Å, as well as a set of 6 "blue" PCA components $B_j$ between 1175 Å $\leq \lambda_{\rm rest} <$ 1220 Å. We then determine the best estimate for the coefficients for the set of red PCA components $r_i$ by fitting them to the red side of the quasar spectra, which we first normalize to unity at $\lambda_{\rm rest} = (1290 \pm 2.5)$ Å. All spectral regions that show contamination by BAL features are masked when estimating the quasar continua. Note that whenever we have no NIR data available the wavelength range is truncated to 1220 Å $\leq \lambda_{\rm rest} \leq$ 1470 Å.

The best set of estimated red coefficients $r_i$ are then projected onto a set of blue coefficients $b_j$ for the blue PCA components by means of a projection matrix $P_{ij}$ determined from the training spectra, i.e.

$$b_j = \sum_{i=1}^{N_{\rm PCA,r}} r_i P_{ij}. \tag{4}$$

The quasar spectra as well as their best estimated continuum model for both the red and blue wavelength side

**Table 3.** NIR properties of our quasar sample.

| object | $z_{\rm Mg\,II}$ | FWHM$_{\rm Mg\,II}$ | $\Delta v$ (Mg II-[C II]) | $M_{\rm BH}$ | $L_{\rm bol}$ | $\lambda_{\rm Edd}$ |
|---|---|---|---|---|---|---|
| | | [km s$^{-1}$] | [km s$^{-1}$] | [$10^9$ M$_\odot$] | [$10^{46}$ erg s$^{-1}$] | |
| PSO J011+09 | $6.458 \pm 0.001$ | $3532 \pm 732$ | $-466 \pm 45$ | $1.20 \pm 0.51$ | $9.14 \pm 1.33$ | $0.58 \pm 0.26$ |
| VDES J0323–4701 | $6.238 \pm 0.006$ | $2335 \pm 2668$ | – | $0.55 \pm 1.26$ | $10.01 \pm 1.58$ | $1.40 \pm 3.20$ |
| VDES J0330–4025 | $6.239 \pm 0.005$ | $7277 \pm 524$ | – | $5.87 \pm 0.89$ | $12.04 \pm 1.13$ | $0.16 \pm 0.03$ |
| PSO J056–16 | $5.975 \pm 0.001$ | $2568 \pm 118$ | $332 \pm 38$ | $0.75 \pm 0.07$ | $12.72 \pm 0.32$ | $1.30 \pm 0.13$ |
| PSO J158–14 | $6.057 \pm 0.001$ | $3013 \pm 173$ | $-481 \pm 21$ | $2.15 \pm 0.25$ | $55.01 \pm 1.62$ | $1.97 \pm 0.23$ |
| PSO J239–07 | $6.114 \pm 0.001$ | $4490 \pm 115$ | $193 \pm 44$ | $3.63 \pm 0.20$ | $31.87 \pm 1.06$ | $0.67 \pm 0.04$ |
| PSO J261+19 | $6.483 \pm 0.004$ | $2591 \pm 398$ | – | $0.67 \pm 0.21$ | $9.77 \pm 1.34$ | $1.12 \pm 0.39$ |
| CFHQS J2100–1715 | $6.082 \pm 0.004$ | $5798 \pm 544$ | – | $3.37 \pm 0.64$ | $9.86 \pm 0.46$ | $0.23 \pm 0.04$ |
| CFHQS J2229+1457 | $6.149 \pm 0.007$ | $5380 \pm 885$ | – | $1.72 \pm 0.62$ | $3.47 \pm 1.05$ | $0.16 \pm 0.07$ |
| PSO J359–06 | $6.164 \pm 0.001$ | $3103 \pm 195$ | $-316 \pm 62$ | $1.66 \pm 0.21$ | $29.04 \pm 0.84$ | $1.35 \pm 0.17$ |

NOTE—The columns show the name of the quasar, its redshift estimate based on the Mg II emission line, the FWHM of the Mg II line, the velocity shift between Mg II and [C II] emission lines, the mass of the central SMBH, as well as the quasar's bolometric luminosity, and Eddington ratio.

are shown in Fig. 10 and Fig. 11 in Appendix C. The predicted continua match the data overall well. However, while estimates of the IGM neutral gas fraction for which this continuum fitting machinery was originally developed (Davies et al. 2018) critically depend on precise continuum estimates, the proximity zone measurements are more robust with respect to uncertainties in the continuum fit (Eilers et al. 2017a,b). The continuum model is predicted to be biased by less than 2% with continuum uncertainties of less than 10% in the wavelength range of interest (see Davies et al. 2018, Fig. 9), which is not sufficient to alter the proximity zone size measurement for any of the quasars.

### 4.4. *Proximity Zone Sizes*

In order to estimate the sizes of the quasars' proximity zones, we adopt the standard definition applied in previous studies (Fan et al. 2006; Willott et al. 2007, 2010; Carilli et al. 2010; Venemans et al. 2015; Mazzucchelli et al. 2017; Eilers et al. 2017a). Namely, we normalize the quasar spectra by their estimated continuum emission, and smooth the continuum normalized flux with a 20 Å-wide (in the observed wavelength frame) boxcar function, which corresponds to a smoothing scale of approximately 1 pMpc or 700 km s$^{-1}$ at $z \sim 6$. The location at which the smoothed continuum-normalized flux drops below the 10% level marks the extent of the proximity zone $R_p$. All continuum-normalized quasar spectra and their proximity zones are shown in Fig. 4.

For the estimate of the proximity zone sizes we take the best available redshift estimate (see § 4.1 and § 4.2). We expect the size of the proximity zone to depend on the luminosity of quasars (e.g. Fan et al. 2006; Bolton & Haehnelt 2007b; Davies et al. 2019b), and thus we normalize the proximity zone measurements to the same fiducial absolute luminosity of $M_{1450} = -27$. Using a radiative transfer simulation to understand the relation between the observed proximity zone sizes and quasar luminosity, we found that

$$R_{p,\,\rm corr} = R_p \times 10^{-0.4(-27-M_{1450})/2.35} \quad (5)$$

best eliminates the dependency on the quasars' luminosity and yields "luminosity-corrected" proximity zone measurements $R_{p,\,\rm corr}$ (Eilers et al. 2017a). Note that this scaling relation depends only marginally on the ionization state of the ambient IGM surrounding the quasars (Eilers et al. 2017a). All proximity zone measurements, as well as the luminosity-corrected estimates, are presented in Table 4.

#### 4.4.1. *Search for Associated Absorption Systems*

We carefully search for any associated absorption systems in the quasar spectra that might prematurely truncate the quasars' proximity zones. This would be the case if a self-shielding Lyman limit system is located within $\lesssim 1000$ km s$^{-1}$ of the quasar, around the edge of its proximity zone (e.g. D'Odorico et al. 2018; Bañados et al. 2019). To this end, we search for strong low-ionization metal absorption lines redwards of the Ly$\alpha$ emission line, which we would expect to find if a self-shielding absorption system is present. We do not find any evidence for such systems in the majority of our data, however, we do find two absorption systems in

**Table 4.** Proximity zone measurements.

| object | $z$ | $z_{\rm line}$ | $M_{1450}$ | $R_p$ [pMpc] | $R_{p,\,\rm corr}$ [pMpc] | notes |
|---|---|---|---|---|---|---|
| PSO J004+17 | $5.8165 \pm 0.0004$ | [C II] | $-26.01$ | $1.15 \pm 0.03$ | $1.70 \pm 0.04$ | - |
| PSO J011+09 | $6.4693 \pm 0.0002$ | [C II] | $-26.85$ | $2.40 \pm 0.01$ | $2.54 \pm 0.01$ | - |
| VDES J0323–4701 | $6.238 \pm 0.006$ | Mg II | $-26.02$ | $1.60 \pm 0.34$ | $2.35 \pm 0.50$ | - |
| VDES J0330–4025 | $6.239 \pm 0.005$ | Mg II | $-26.42$ | $1.14 \pm 0.30$ | $1.43 \pm 0.38$ | - |
| PSO J056–16 | $5.9670 \pm 0.0003$ | [C II] | $-26.72$ | $0.75 \pm 0.02$ | $0.84 \pm 0.02$ | pDLA |
| PSO J158–14 | $6.0681 \pm 0.0001$ | [C II] | $-27.41$ | $1.93 \pm 0.01$ | $1.64 \pm 0.01$ | - |
| SDSS J1143+3808 | $5.8367 \pm 0.0010$ | CO(6–5) | $-26.69$ | $4.27 \pm 0.07$ | $4.82 \pm 0.08$ | - |
| PSO J239–07 | $6.1098 \pm 0.0002$ | [C II] | $-27.46$ | $1.27 \pm 0.01$ | $1.06 \pm 0.01$ | BAL |
| PSO J261+19 | $6.483 \pm 0.004$ | Mg II | $-25.69$ | $2.80 \pm 0.23$ | $4.68 \pm 0.38$ | - |
| PSO J265+41 | $6.0262 \pm 0.0002$ | [C II] | $-25.56$ | $1.04 \pm 0.01$ | $1.82 \pm 0.02$ | BAL |
| CFHQS J2100–1715 | $6.0806 \pm 0.0011$ | [C II] | $-25.55$ | $0.36 \pm 0.07$ | $0.63 \pm 0.12$ | - |
| CFHQS J2229+1457 | $6.1517 \pm 0.0005$ | [C II] | $-24.78$ | $0.48 \pm 0.03$ | $1.15 \pm 0.07$ | - |
| PSO J359–06 | $6.1718 \pm 0.0001$ | [C II] | $-26.79$ | $2.80 \pm 0.01$ | $3.04 \pm 0.01$ | - |

Note—The columns show the name of the quasar, its best redshift estimate, its absolute magnitude $M_{1450}$, as well as the size of the proximity zone and its magnitude corrected value. The last column indicates whether the quasar has broad absorption lines (BAL) or associated absorption systems, which might have contaminated the proximity zones.

the spectra of PSO J004+17 and PSO J056–16, shown in Fig. 5.

The spectrum of PSO J004+17 (top panel of Fig. 5) shows an associated absorption system located within the quasar's proximity zone directly at the systemic redshift of the quasar, i.e. $z_{\rm abs} \approx 5.8165$, possibly due to the host galaxy itself. However, this system only shows high-ionization absorption lines, such as the doublets N V at the rest-frame wavelengths $\lambda = 1238$ Å and $\lambda = 1242$ Å, and Si IV at $\lambda = 1393$ Å and $\lambda = 1402$ Å. We do not find any evidence for low-ionization lines, indicating that the absorption system is unlikely to be self-shielding. Additionally, the spectrum shows clear flux transmission bluewards of the absorption system, which indicates that the proximity zone extends beyond this absorber. Thus we can exclude a premature truncation of the quasar's proximity zone due to this absorption system.

The spectrum of PSO J056–16 shows a proximate damped Ly$\alpha$ absorption (pDLA) system in front of the quasar along our line-of-sight at $z_{\rm abs} \approx 5.9369$, i.e. with a velocity offset of $\Delta v \approx 1297\,{\rm km\,s^{-1}}$, which is shown in the bottom panel of Fig. 5. This system clearly shows low-ionization absorption lines such as Si II and O I, has a high column density (a fit by eye indicates $N_{\rm HI} \gtrsim 10^{20}\,{\rm cm^{-2}}$) and is thus optically thick, causing a premature truncation of the quasar's proximity zone. We searched the dust-continuum map of this quasar shown in Fig. 8 in Appendix A for the presence of a second continuum source that could be associated with the pDLA, but we did not detect any other sources in the vicinity of this quasar, presumably due to their low continuum luminosity.

Furthermore, two quasars in our sample, i.e. PSO J239–07 and PSO J265+41, will be excluded from any further analyses of their proximity zone sizes, since they exhibit BAL features in their optical/NIR spectra (see Fig. 3), which might contaminate or prematurely truncate their proximity zones.

### 4.5. *Star Formation Rates*

We convert the integrated fluxes $F_{\rm line}$ of the sub-mm emission lines into line luminosities by means of

$$\frac{L_{\rm line}}{L_\odot} = 1.04 \times 10^{-3} \frac{F_{\rm line}}{\rm Jy\,km\,s^{-1}} \frac{\nu_{\rm obs}}{\rm GHz} \left(\frac{D_{\rm L}}{\rm Mpc}\right)^2, \quad (6)$$

where $D_{\rm L}$ represents the luminosity distance and $\nu_{\rm obs}$ is the mean observed frequency of the line (see e.g. Carilli & Walter 2013).

Following De Looze et al. (2014) we estimate the SFR within the quasars' host galaxies based on their [C II] line luminosities via

$$\log \frac{\rm SFR_{[C\,II]}}{M_\odot\,{\rm yr^{-1}}} = -8.52 + 1.18 \times \log \frac{L_{\rm [C\,II]}}{L_\odot}. \quad (7)$$

This relation has been derived based on $z > 0.5$ galaxies and has an estimated scatter of 0.4 dex.

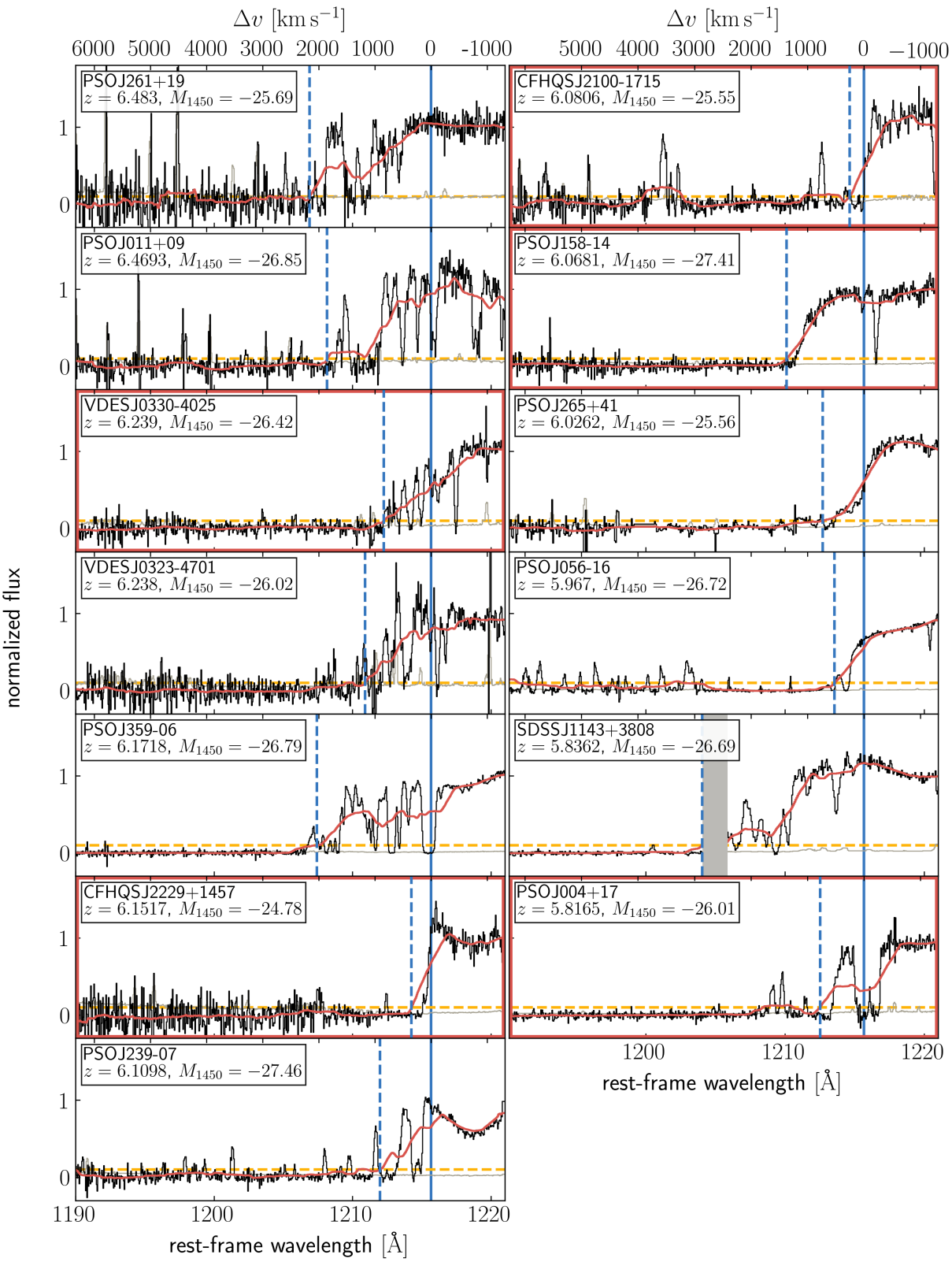


**Figure 4. Proximity zones of all quasars in our sample.** The continuum-normalized fluxes with uncertainties are shown in black and grey, respectively, and are inverse-variance smoothed with a 2 pixel filter. The blue solid and dashed lines indicate the systemic redshift of the quasar, as well as the edge of the proximity zone, respectively, which is defined to end where the smoothed continuum-normalized flux (red curves) drops below the 10% flux level indicated by the yellow dashed line. The red frames show quasars with very small proximity zones. The DEIMOS detector gap in the spectrum of SDSS 1143+3803 is masked by the grey shaded region.

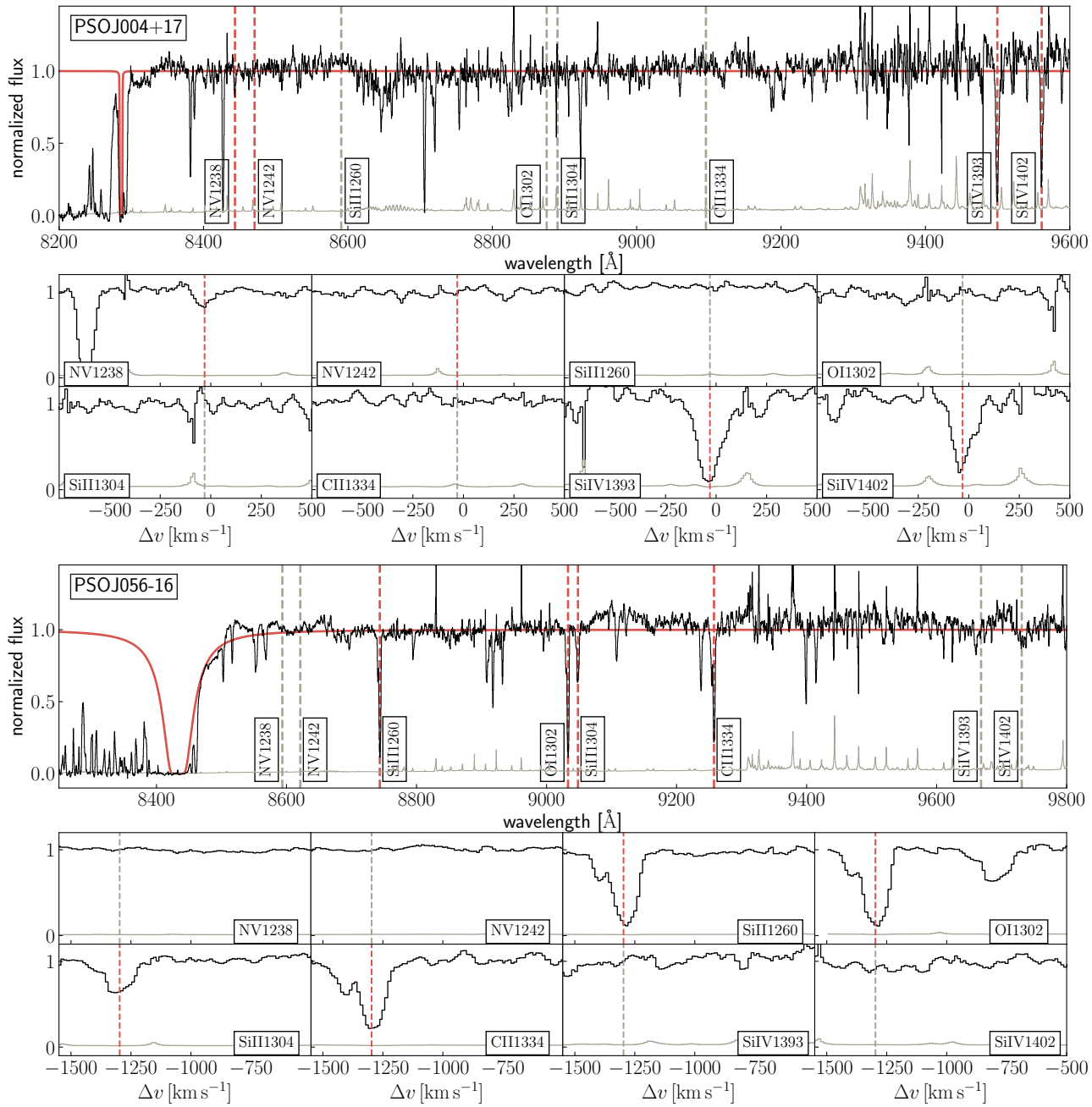


**Figure 5.** Optical quasar spectra showing absorption systems in the vicinity of the two quasars PSO J004+17 (*top*) and PSO J056 − 16 (*bottom*). Symbolic absorption systems with parameters $\log N_{\rm HI} = 17\,{\rm cm}^{-2}$ and $b = 25\,{\rm km\,s}^{-1}$, as well as $\log N_{\rm HI} = 20.4\,{\rm cm}^{-2}$ and $b = 25\,{\rm km\,s}^{-1}$, are shown as the red curves in the top and bottom panel, respectively. The detected ionic metal absorption lines are indicated by the red dashed lines, whereas the expected locations of absorption lines that we did not detect in the spectrum are indicated as grey dashed lines.

An alternative method to estimate the SFR within the quasars' host galaxies is based on the dust continuum flux. To this end, we estimate the dust continuum emission as a modified black body (e.g. Dunne et al. 2000; Beelen et al. 2006), i.e.

$$L_{\nu,\,\rm dust} = \frac{2h\nu^3}{c^2}\kappa_\nu(\beta)\frac{M_{\rm dust}}{\exp[h\nu/k_{\rm b}T_{\rm dust}]-1} \qquad (8)$$

with a dust temperature of $T_{\rm dust} = 47\,{\rm K}$, and the opacity law $\kappa_\nu(\beta) = 0.77(\nu/352\,{\rm GHz})^\beta\,{\rm cm}^2\,{\rm g}^{-1}$ with the (dust) emissivity index $\beta = 1.6$. We obtain an estimate of the dust mass by means of the dust continuum flux $F_{\rm cont}$ measured around the rest-frame frequency $\nu$ (Venemans

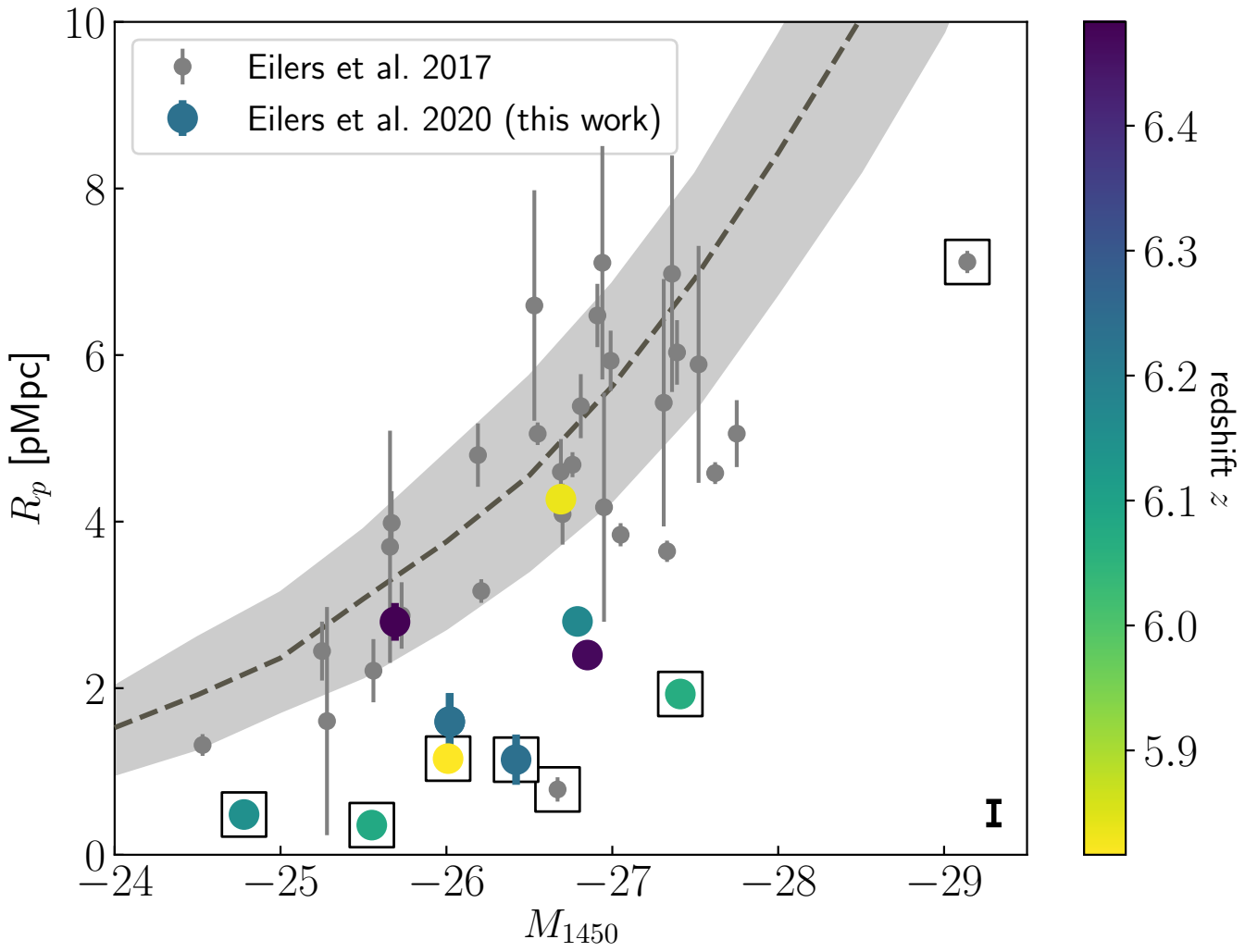


**Figure 6.** Proximity zone sizes $R_p$ as a function of the quasars' absolute magnitude $M_{1450}$. Our new measurements are shown as colored data points, whereas the grey square data points shows previous work (Eilers et al. 2017a). The grey dashed line and shaded region represents the median and 68th percentile of the distribution of 400 simulated proximity zones from radiative transfer simulations at $z = 6$ and $\log t_Q = 7.5$ yr (see Davies et al. 2016; Eilers et al. 2017a, for details), respectively. The seven quasars with extremely small proximity zones are indicated by the black boxes. The black errorbar in the bottom right indicates the systematic uncertainty on the $R_p$ measurements with sub-mm redshifts, assuming a systematic uncertainty on the sub-mm redshift estimates of $\Delta v = 100\,\mathrm{km\,s^{-1}}$.

et al. 2012), i.e.

$$M_{\mathrm{dust}} = \frac{F_{\mathrm{cont}}\, D_{\mathrm{L}}^2}{(1+z)\kappa_\nu(\beta) B(\nu, T_{\mathrm{dust}})}, \tag{9}$$

where $B(\nu, T_{\mathrm{dust}})$ is the Planck function. The IR-luminosity $L_{\mathrm{IR}}$ is estimated by integrating Eqn. 8 over the solid angle and between $3\,\mu$m and $1100\,\mu$m in the rest-frame (e.g. Kennicutt & Evans 2012).

We obtain a dust-based SFR estimate following Kennicutt & Evans (2012) via the scaling relation

$$\frac{\mathrm{SFR_{IR}}}{\mathrm{M_\odot\,yr^{-1}}} = 1.49 \times 10^{-10} \frac{L_{\mathrm{IR}}}{L_\odot}. \tag{10}$$

All derived quantities are shown in Table 5. Note that the statistical uncertainties on these values are small, but in practice the uncertainties are dominated by the scatter of $0.4 - 0.5$ dex in the scaling relations (Eqn. 7 and Eqn. 10).

### 4.6. *Notes on Individual Objects*

In Fig. 6 we show all proximity zone measurements that are not prematurely truncated or potentially contaminated by BAL features, as a function of the quasars' absolute magnitude $M_{1450}$. All quasars in our data sample show smaller proximity zone sizes than the expected average given their magnitude, which results from our selection criteria aiming to target young quasars. Five

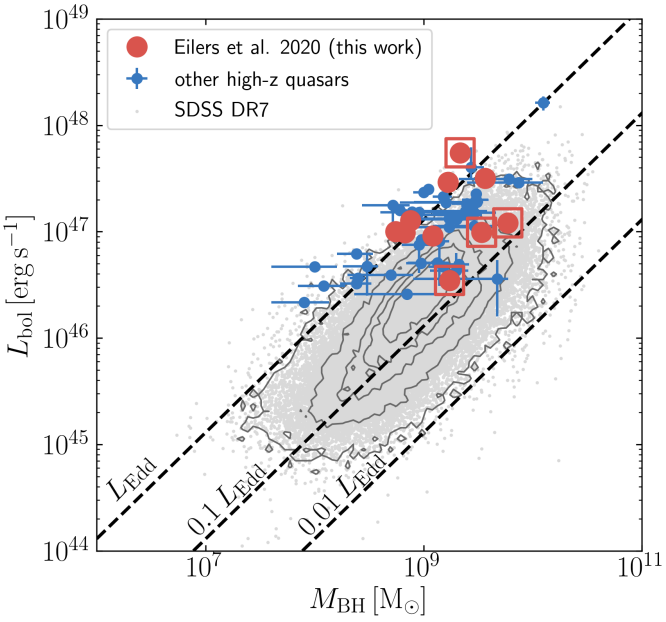


**Figure 7.** Relation between $L_{\rm bol}$ and $M_{\rm BH}$ for our new measurements (red) compared to a quasar sample at $0.4 \lesssim z \lesssim 2.2$ from SDSS DR7 (grey), as well as several other $z \gtrsim 5.8$ quasars (blue). The red boxes indicate quasars with short lifetimes. The black dashed curves show regions with constant Eddington luminosity.

**Table 5.** Properties of the quasar sample derived from the dust continuum and [C II] emission.

| object | $\log L_{\rm IR}$ | $M_{\rm dust}$ | SFR$_{\rm [C\,II]}$ | SFR$_{\rm dust}$ |
|---|---|---|---|---|
| | [L$_\odot$] | $10^7$ [M$_\odot$] | [M$_\odot$ yr$^{-1}$] | [M$_\odot$ yr$^{-1}$] |
| PSOJ004+17 | 12.28 | 8.7 | 170 | 290 |
| PSOJ011+09 | 12.40 | 11.3 | 130 | 370 |
| PSOJ056-16 | 11.49 | 1.4 | 40 | 50 |
| PSOJ158-14 | 12.91 | 36.4 | 1290 | 1200 |
| SDSSJ1143+3808 | 11.26 | 0.8 | – | 30 |
| PSOJ239-07 | 11.68 | 2.2 | 80 | 70 |
| PSOJ261+19 | $< 11.65$ | $< 2.0$ | – | $< 70$ |
| PSOJ265+41 | 12.93 | 38.7 | 590 | 1270 |
| CFHQSJ2100-1715 | 12.16 | 6.5 | 170$^b$ | 210 |
| CFHQSJ2229+1457 | 12.18 | 6.9 | 60$^c$ | 230 |
| PSOJ359-06 | 12.14 | 6.3 | 280 | 210 |

Note—The columns show the name of the quasar, the estimated IR luminoisty, and dust mass, as well as the inferred SFR of the quasars' host galaxies by means of the [C II] emission line or the dust continuum. The SFR$_{\rm [CII]}$ for CFHQS J2100–1715 and CFHQS J2229+1457 were derived by (*a*) Decarli et al. (2018) and (*b*) Willott et al. (2015), respectively.

quasars that show no associated absorption systems or broad absorption lines, exhibit extremely small proximity zones with $R_{p,\,\rm corr} < 2$ pMpc. These five quasars plus two from our previous study (Eilers et al. 2017a), which are marked with boxes in Fig. 6, indicate very short quasar lifetimes, i.e. $t_{\rm Q} \lesssim 10^5$ yr, which will be analyzed in more detail in Paper II.

Fig. 7 shows the bolometric luminosity as a function of the quasars' black hole masses. Our new measurements are compared to a low redshift quasar sample of $\gtrsim 75,000$ objects from the SDSS Data Release 7 (DR7) (Shen et al. 2011; Wang et al. 2015), as well as to several other $z \gtrsim 5.8$ quasars (Jiang et al. 2007; Willott et al. 2010; De Rosa et al. 2011, 2014; Wu et al. 2015; Mazzucchelli et al. 2017; Bañados et al. 2018). The quasars with very small proximity zones marked with red boxes do not populate a special region in the parameter space.

#### 4.6.1. *Quasars with Particularly Small Proximity Zones*

*PSO J004+17*

This object has a very small proximity zone of $R_p = 1.15 \pm 0.03$ pMpc ($R_{p,\,\rm corr} = 1.70 \pm 0.04$ pMpc). Although we find a high-ion absorption system within the quasar's proximity zone, it is not optically thick, and thus could not have prematurely truncated the proximity zone (see § 4.4.1). The redshift of the absorption system coincides with the quasar's systemic redshift and might thus be due to the quasar's host galaxy. The dust continuum map shown in Fig. 8 reveals two other continuum sources in the vicinity of this quasar.

*VDES J0330–4025*

This object exhibits a very small proximity zone of $R_p = 1.14 \pm 0.30$ pMpc ($R_{p,\,\rm corr} = 1.43 \pm 0.38$ pMpc). It also has the largest black hole mass within our sample, i.e. $M_{\rm BH} = (5.87 \pm 0.89) \times 10^9\,M_\odot$.

*PSO J158–14*

This quasar, discovered both by Chehade et al. (2018) and Bañados et al. in prep., shows a small proximity zone of $R_p = 1.93 \pm 0.01$ pMpc ($R_{p,\,\rm corr} = 1.64 \pm 0.01$ pMpc). Interestingly, the quasar has a very strong dust continuum emission and [C II] emission line, which is one of the brightest [C II] lines detected to date (Decarli et al. 2018), i.e. $F_{\rm line} = 7.18 \pm 0.33$ Jy km s$^{-1}$. The derived star formation rate of approximately $1200\,M_\odot\,{\rm yr}^{-1}$ suggests the presence of a coeval starburst with the SMBH growth. Furthermore, we estimate a large bolometric luminosity of $L_{\rm bol} = (55.01 \pm 1.62) \times 10^{46}$ erg s$^{-1}$ and a very high Eddington ratio of $\lambda_{\rm Edd} = 1.97 \pm 0.23$. The Mg II emission line is highly blueshifted with respect to the systemic

redshift of the quasar, i.e. $\Delta v = -481 \pm 21\,\mathrm{km\,s^{-1}}$, suggesting strong internal motions within the BLR.

*CFHQS J2100–1715*

This quasar exhibits the smallest proximity zone $R_p = 0.36 \pm 0.07$ pMpc ($R_{p,\,\mathrm{corr}} = 0.63 \pm 0.12$ pMpc) detected to date with no signs of contamination from associated absorption systems. Decarli et al. (2017) reported the detection of a companion galaxy at a projected separation of $\sim 60$ kpc, suggesting that the two objects might be at an early stage of interaction. Its spectrum shows a very red spectral slope (Willott et al. 2009).

*CFHQS J2229+1457*

This quasar's small proximity zone has been confirmed in this study, i.e. $R_p = 0.48 \pm 0.03$ pMpc ($R_{p,\,\mathrm{corr}} = 1.15 \pm 0.07$ pMpc). Its X-Shooter spectrum did not reveal any associated absorption systems that could truncate or contaminate its proximity zone. Note that the black hole mass measurement for this object should be taken with caution, because the Mg II emission line falls on top of a telluric feature. Our measurement differs from a previous measurement by Willott et al. (2010) who made use of a lower resolution spectrum ($R \approx 520$) observed with NIRI/Gemini by more than one order of magnitude.

#### 4.6.2. *Remaining Objects*

*PSO J011+09*

This object the second highest-redshift quasar in our data sample. Its Mg II emission line is highly blueshifted, i.e. $\Delta v = -466 \pm 45\,\mathrm{km\,s^{-1}}$, with respect to the [C II] systemic redshift.

*VDES J0323–4701*

It has been speculated that this quasar as well as VDES J0330–4025 might lie in an overdense region of the universe, since they are located within 10 degrees on the sky (Reed et al. 2017). The new, very similar redshift estimates for both objects based on their Mg II emission lines of $z \approx 6.238$ with a very small velocity difference of $\Delta v \approx 56\,\mathrm{km\,s^{-1}}$ supports this hypothesis. However, the NIR spectrum of this object has a very low SNR and thus these estimates should be taken with caution.

*PSO J056–16*

As shown in Fig. 5 this quasar's proximity zone has been prematurely truncated due to a pDLA along our line-of-sight. Thus, we exclude this object from any further analysis of its proximity zone. The estimated large Eddington ratio of $\lambda_{\mathrm{Edd}} = 1.30 \pm 0.13$ indicates that this quasar has a high accretion rate.

*SDSS J1143+3803*

Based on the new redshift estimate from the CO(6–5) emission line ($z_{\mathrm{CO(6-5)}} \approx 5.8367$), which is significantly higher than the preliminary estimate from the Ly$\alpha$ emission line ($z_{\mathrm{Ly}\alpha} \approx 5.805$), this quasar has the largest proximity zone ($R_p = 4.27 \pm 0.07$ pMpc) in our sample. Unfortunately, the end of its zone falls right in between the two DEIMOS detectors, which are separated by a $\Delta\lambda = 11$ Å wide gap, causing the uncertainty on the proximity zone measurement to be underestimated.

*PSO J239–07*

Although this quasar exhibits a very small proximity zone, i.e. $R_p = 1.27 \pm 0.01$ pMpc, the broad absorption line features detected in its optical/NIR spectrum might have contaminated its zone. Thus, we exclude this object from any further analysis. The dust continuum map shown in Fig. 8 shows two other continuum sources in the vicinity of this quasar.

*PSO J261+19*

This quasar is the highest redshift object in our sample. We could not detect any line nor continuum emission associated with its host galaxy (see Fig. 1 and Fig. 8), indicating that its emission is very faint, i.e. $F_{\mathrm{cont}} < 0.15$ mJy. Its NIR spectrum suggests a high Eddington ratio of $\lambda_{\mathrm{Edd}} = 1.12 \pm 0.39$.

*PSO J265+41*

This object has been discovered by Bañados et al. in prep. It is a BAL quasar, and has thus been eliminated from our analysis about proximity zones, since its absorption features might contaminate the proximity zone. This quasar shows a very bright [C II] line ($F_{\mathrm{line}} = 3.72 \pm 0.78$), as well as a bright dust continuum emission ($F_{\mathrm{cont}} = 3.13 \pm 0.10$), suggesting a highly star-forming ($\mathrm{SFR} = 590 - 1270\,\mathrm{M_\odot\,yr^{-1}}$) quasar host galaxy.

*PSO J359–06*

This object has a bright [C II] emission line, i.e. $F_{\mathrm{line}} = 1.93 \pm 0.12\,\mathrm{Jy\,km\,s^{-1}}$. Its NIR spectrum suggests a high Eddington ratio of $\lambda_{\mathrm{Edd}} = 1.35 \pm 0.17$.

### 4.7. *Fraction of Young Quasars*

In our previous study we discovered three young quasars in a parent sample of 34, which implies a fraction of young quasars within the quasar population at large of $f_{\mathrm{young}} \approx 3/34 \approx 9\%$ (Eilers et al. 2017a). For a majority of objects in this sample we had precise redshift estimates and good spectroscopic data, and hence

the young population within this data set is likely to be complete.

Assuming that the five objects mentioned in § 4.6.1 all have short quasar lifetimes we now know a total of seven young objects. Please be reminded that one of the here analyzed objects was already previously identified to have a short quasar lifetime (Eilers et al. 2017a). Given a quasar sample of approximately 150 objects, i.e. the combined $\approx$ 120 quasars from the parent sample of this study (§ 2) and the 34 objects from Eilers et al. (2017a), we obtain an estimated fraction of young quasars $f_{\rm young} \approx 7/150 \approx 5\%$. However, this estimate likely represents a lower limit, since there might still be more quasars with short lifetimes within the remaining sample for which we did not conduct follow-up observations and thus no precise redshift estimates exist to date.

Thus, we conclude that the fraction of young quasars within the whole quasar population in the early universe is $5\% \lesssim f_{\rm young} \lesssim 9\%$.

## 5. SUMMARY & CONCLUSIONS

We perform a multi-wavelength analysis to systematically detect and characterize high-redshift quasars that are likely to be very young, as indicated by their small proximity zones. We analyze 13 quasars at $5.8 \lesssim z \lesssim 6.5$, and determine precise redshift estimates by means of their [C II] or CO $(6-5)$ emission lines arising from the cold gas of the host galaxy observed with ALMA and NOEMA, or based on their Mg II emission line from the NIR spectra observed with VLT/X-Shooter, if no sub-mm data is available. These new redshift estimates allow us to precisely measure the size of the proximity zones of the quasars, which we will use in a subsequent follow-up paper to determine their lifetimes (Paper II). Additionally, the deep optical and NIR spectra we obtained from VLT/X-Shooter and Keck/DEIMOS for the quasar sample allow us to exclude a contamination of the proximity zone due to associated absorption systems or broad absorption lines, and enable measurements of the black hole masses, as well as the Eddington ratio of their accretion.

The main results of this study are:

1. We find five quasars (PSO J004+17, VDES J0330–4025, PSO J158–14, CFHQS J2100–1715, and CFHQS J2229+1457) that exhibit particularly small proximity zones, i.e. $R_{p,\,\rm corr} \lesssim 2$ pMpc, and thus likely indicate very short quasar lifetimes, i.e. $t_{\rm Q} \lesssim 10^5$ yr. One of these five objects, CFHQS J2229+1457, has previously been identified as a very young quasar (Eilers et al. 2017a).

2. The quasar CFHQS J2100–1715 exhibits the smallest proximity zone detected to date, i.e. $R_{p,\,\rm corr} = 0.63 \pm 0.12$ pMpc. Additionally, its companion galaxy (Decarli et al. 2017) might indicate that this system is at an early stage of interaction.

3. Our previous work revealed three young quasars in a sample of 34 objects (Eilers et al. 2017a). For this study, we analyzed $\approx$ 120 quasar spectra, and chose the most promising 13 candidates to follow-up. We discover five young quasars in this data set, one of which was previously known. This allows us to constrain the fraction of young quasars within the high-redshift quasar population at large to be $5\% \lesssim f_{\rm young} \lesssim 9\%$.

4. We determine the spectral properties of the quasars in our sample, such as black hole masses, the velocity shifts of the emission lines, and the Eddington ratios of the accretion of the SMBHs. For several objects in the sample we measure large Eddington ratios, i.e. $\lambda_{\rm Edd} \gtrsim 1$, which indicate high mass accretion rates at the Eddington limit. The estimated black hole masses, derived from fitting the single-epoch Mg II region, vary between $M_{\rm BH} \approx 6 \times 10^8 - 6 \times 10^9\,M_\odot$.

5. We measure the line luminosities of the [C II] emission lines and find one particularly bright quasar, i.e. PSO J158–14, with a luminosity of $L_{\rm [C\,II]} \approx 7.19 \times 10^9\,L_\odot$. The inferred high star formation rate of $1200 - 1290\,M_\odot\,{\rm yr}^{-1}$ suggests the presence of a starburst within its host galaxy coeval to the SMBH growth. This quasar represents an ideal target for high-resolution imaging with ALMA to study star formation and the ISM in the very early universe, and search for any signs of mergers, outflows, and feedback.

Our analysis presents a first step towards a systematic study of the lifetimes of high-redshift quasars based on their proximity zone sizes. In future work we will determine the lifetime estimates for this quasar sample, as well as a statistical estimate of the lifetime of the quasar population at large by means of the estimated fraction of young quasars. This will enable us to analyze the evolution of quasar and host galaxy properties with the quasar lifetime, and further study the accretion behaviour of SMBHs in the early universe.

*Software:* CASA (McMullin et al. 2007), GILDAS (http://www.iram.fr/IRAMFR/GILDAS),PypeIt(DOI: 10.5281/zenodo.3506873), numpy (van der Walt et al. 2011), scipy (Jones et al. 2001), matplotlib (Hunter 2007), astropy (The Astropy Collaboration et al. 2018)

The authors would like to thank Sarah Bosman for helpful feedback on the manuscript.

This paper makes use of the following ALMA data: ADS/JAO.ALMA#2017.1.00332.S. ALMA is a partnership of ESO (representing its member states), NSF (USA) and NINS (Japan), together with NRC (Canada), MOST and ASIAA (Taiwan), and KASI (Republic of Korea), in cooperation with the Republic of Chile. The Joint ALMA Observatory is operated by ESO, AUI/NRAO and NAOJ.

This work is based on observations carried out under project number W17EQ and W18EF with the IRAM NOEMA Interferometer [30m telescope]. IRAM is supported by INSU/CNRS (France), MPG (Germany) and IGN (Spain). RD and ACE thank Charlene Lefevre for her support in the IRAM data calibration.

This work is based on observations collected at the European Organisation for Astronomical Research in the Southern Hemisphere under ESO programmes 096.A-0418, 097.B-1070, 098.B-0537, and 101.B-02720.

Some of the data presented in this paper were obtained at the W.M. Keck Observatory, which is operated as a scientific partnership among the California Institute of Technology, the University of California and the National Aeronautics and Space Administration. The Observatory was made possible by the generous financial support of the W.M. Keck Foundation.

The authors wish to recognize and acknowledge the very significant cultural role and reverence that the summit of Mauna Kea has always had within the indigenous Hawaiian community. We are most fortunate to have the opportunity to conduct observations from this mountain.

ACE and F. Wang acknowledge support by NASA through the NASA Hubble Fellowship grant #HF2-51434 and #HST-HF2-51448.001-A awarded by the Space Telescope Science Institute, which is operated by the Association of Universities for Research in Astronomy, Inc., for NASA, under contract NAS5-26555.

BPV and MN acknowledge funding through the ERC grant "Cosmic Gas".

This publication has received funding from the European Unions Horizon 2020 research and innovation programme under grant agreement No 730562 [RadioNet].

# APPENDIX

## A. DUST CONTINUUM MAPS

The dust continuum maps constructed from the two ALMA bandpasses without the [C II] emission line, or the line-free channels from NOEMA are shown in Fig. 8. We find two continuum sources in close (projected) vicinity to the quasars PSO J004+17 and PSO J239–07.

## B. MG II EMISSION LINE FITS

In order to measure the black hole masses of the quasar, we fit the width of the Mg II emission line as described in § 4.2. The best fits to the Mg II emission lines are shown in Fig. 9.

## C. QUASAR CONTINUUM NORMALIZATION

In § 4.3 we described our method to estimate the intrinsic quasar continua. We show the best estimate for each quasar spectrum in Fig. 10 and Fig. 11.

# REFERENCES

Adelberger, K. L. 2004, ApJ, 612, 706

Bañados, E., Venemans, B. P., Decarli, R., et al. 2016, ApJS, 227, 11

Bañados, E., Venemans, B. P., Mazzucchelli, C., et al. 2018, Nature, 553, 473

Bañados, E., Rauch, M., Decarli, R., et al. 2019, ApJ, 885, 59

Bajtlik, S., Duncan, R. C., & Ostriker, J. P. 1988, The Astrophysical Journal, 327, 570

Beelen, A., Cox, P., Benford, D. J., et al. 2006, ApJ, 642, 694

Bolton, J. S., & Haehnelt, M. G. 2007a, Monthly Notices of the Royal Astronomical Society, 381, L35

—. 2007b, Monthly Notices of the Royal Astronomical Society, 374, 493

Bolton, J. S., Haehnelt, M. G., Warren, S. J., et al. 2011, MNRAS, 416, L70

Bosman, S. E. I., Kakiichi, K., Meyer, R. A., et al. 2019, arXiv e-prints, arXiv:1912.11486

Carilli, C. L., & Walter, F. 2013, ARA&A, 51, 105

Carilli, C. L., Wang, R., Fan, X., et al. 2010, ApJ, 714, 834

Cen, R., & Safarzadeh, M. 2015, Astrophysical Journal Letters, 798, L38

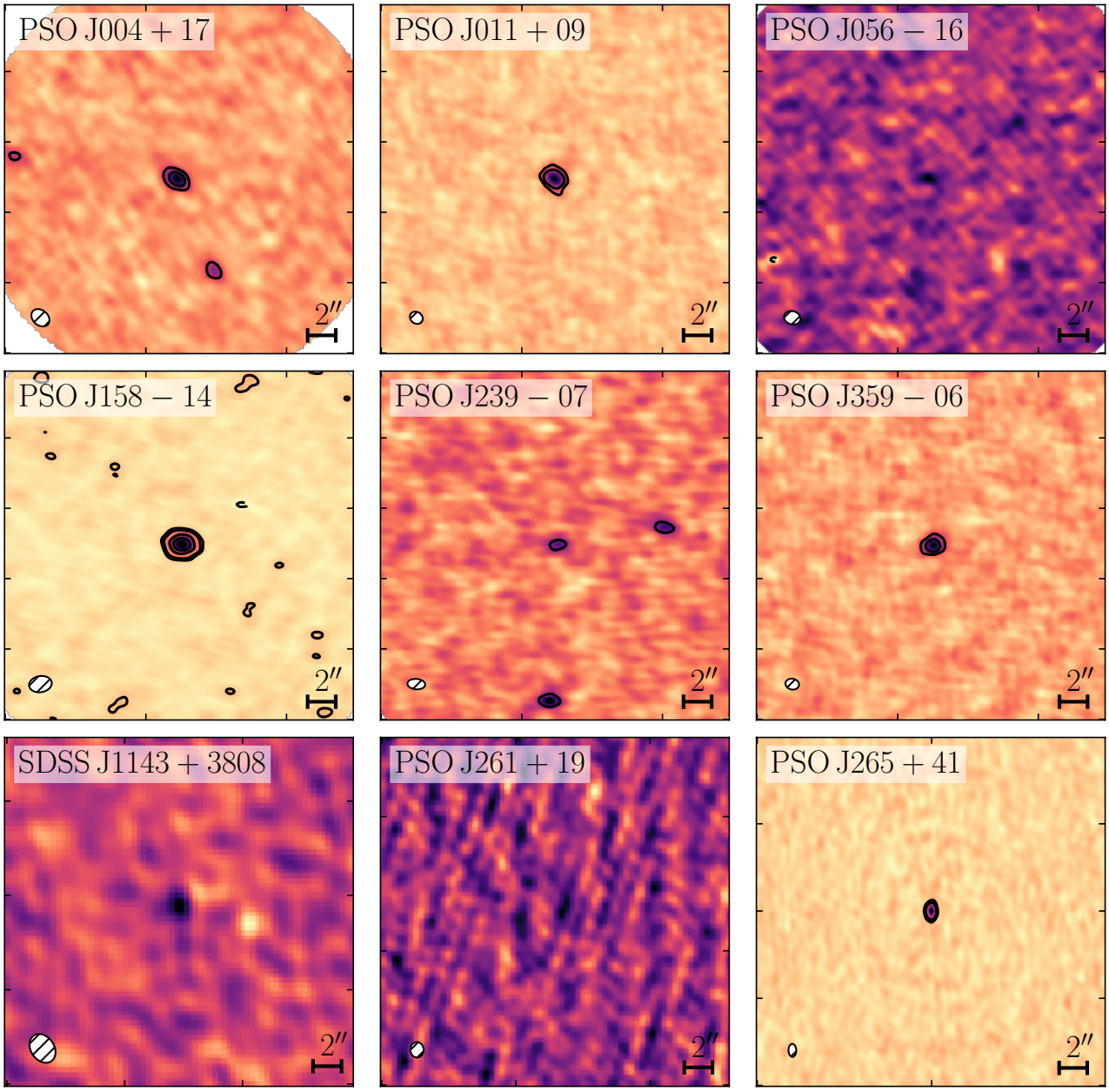


**Figure 8. Dust continuum maps.** The six quasars in the top and middle row show ALMA observations, whereas the bottom row shows our NOEMA data. Each panel is $25'' \times 25''$ in size. Solid and dashed lines show the $\pm 0.5, 1, 3, 5, 7, 9\sigma$ isophotes.


Chehade, B., Carnall, A. C., Shanks, T., et al. 2018, MNRAS, 478, 1649

Clough, S. A., Shephard, M. W., Mlawer, E. J., et al. 2005, JQSRT, 91, 233

Conroy, C., & White, M. 2013, The Astrophysical Journal, 762, 70

Davies, F. B., Furlanetto, S. R., & McQuinn, M. 2016, MNRAS, 457, 3006

Davies, F. B., Hennawi, J. F., & Eilers, A.-C. 2019a, ApJL, 884, L19

—. 2019b, MNRAS, 2958

Davies, F. B., Hennawi, J. F., Bañados, E., et al. 2018, ApJ, 864, 143

De Looze, I., Cormier, D., Lebouteiller, V., et al. 2014, A&A, 568, A62

De Rosa, G., Decarli, R., Walter, F., et al. 2011, The Astrophysical Journal, 739, 56

De Rosa, G., Venemans, B. P., Decarli, R., et al. 2014, The Astrophysical Journal, 790, 145

Decarli, R., Walter, F., Venemans, B. P., et al. 2017, Nature, 545, 457

—. 2018, ApJ, 854, 97

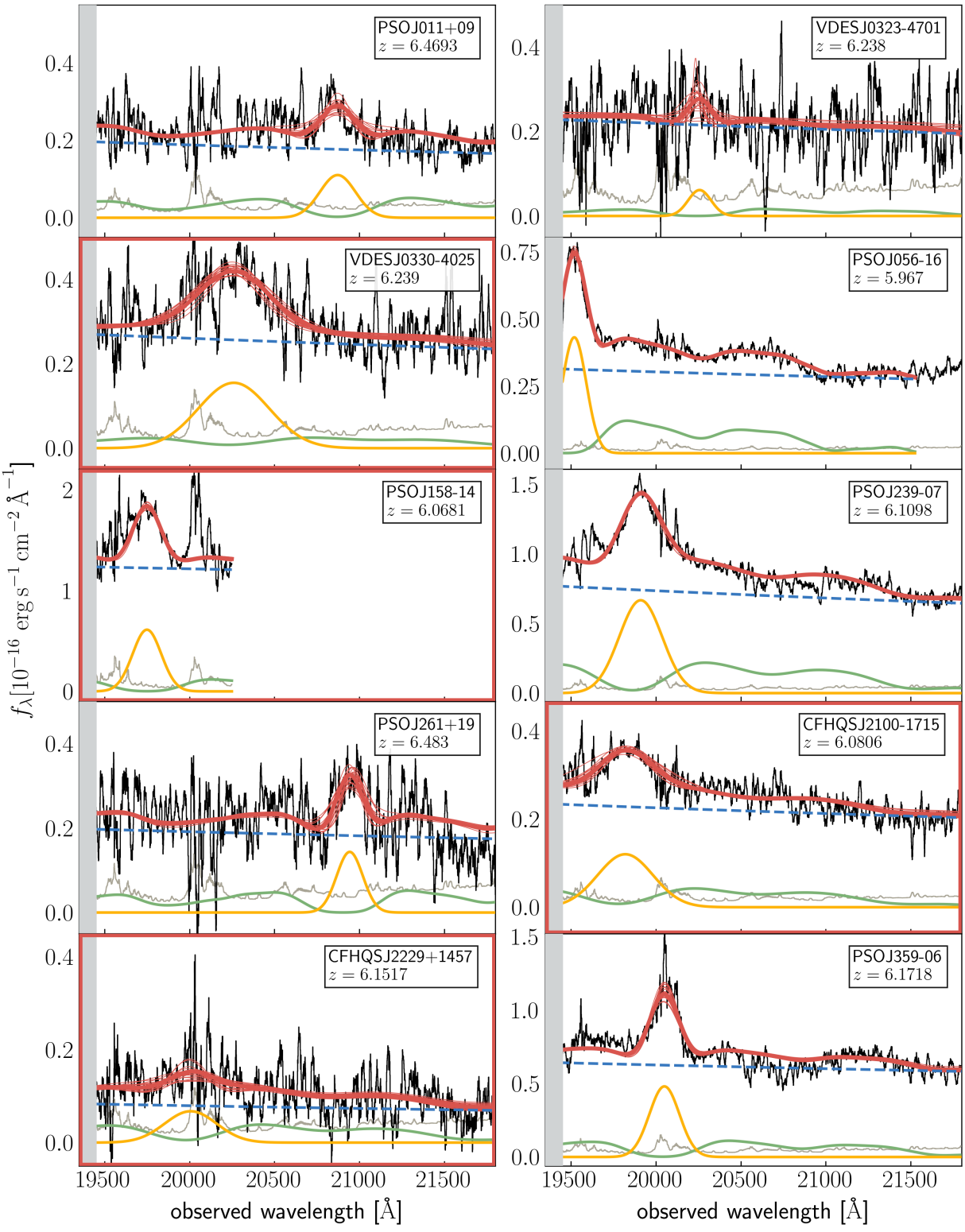


**Figure 9. Best fits to the Mg II emission lines.** We show all quasars in our sample that have NIR spectral coverage and their Mg II line does not fall into a region of high telluric absorption. The spectra around Mg II at $\lambda_{\rm rest} = 2798$ Å and the corresponding noise vector have been inverse-variance smoothed with a 20 pixel filter and are shown in black and grey, respectively. The fit to the quasar emission (red curve), as well as its individual components are shown as the colored curves, i.e. a power-law continuum (blue dashed), the smoothed iron template (green), and a Gaussian for the Mg II emission line. Regions with large telluric absorption have been masked by the grey regions. The faint red lines show draws from the posterior distribution. The red frames show quasars that exhibit very small proximity zones and short lifetimes.

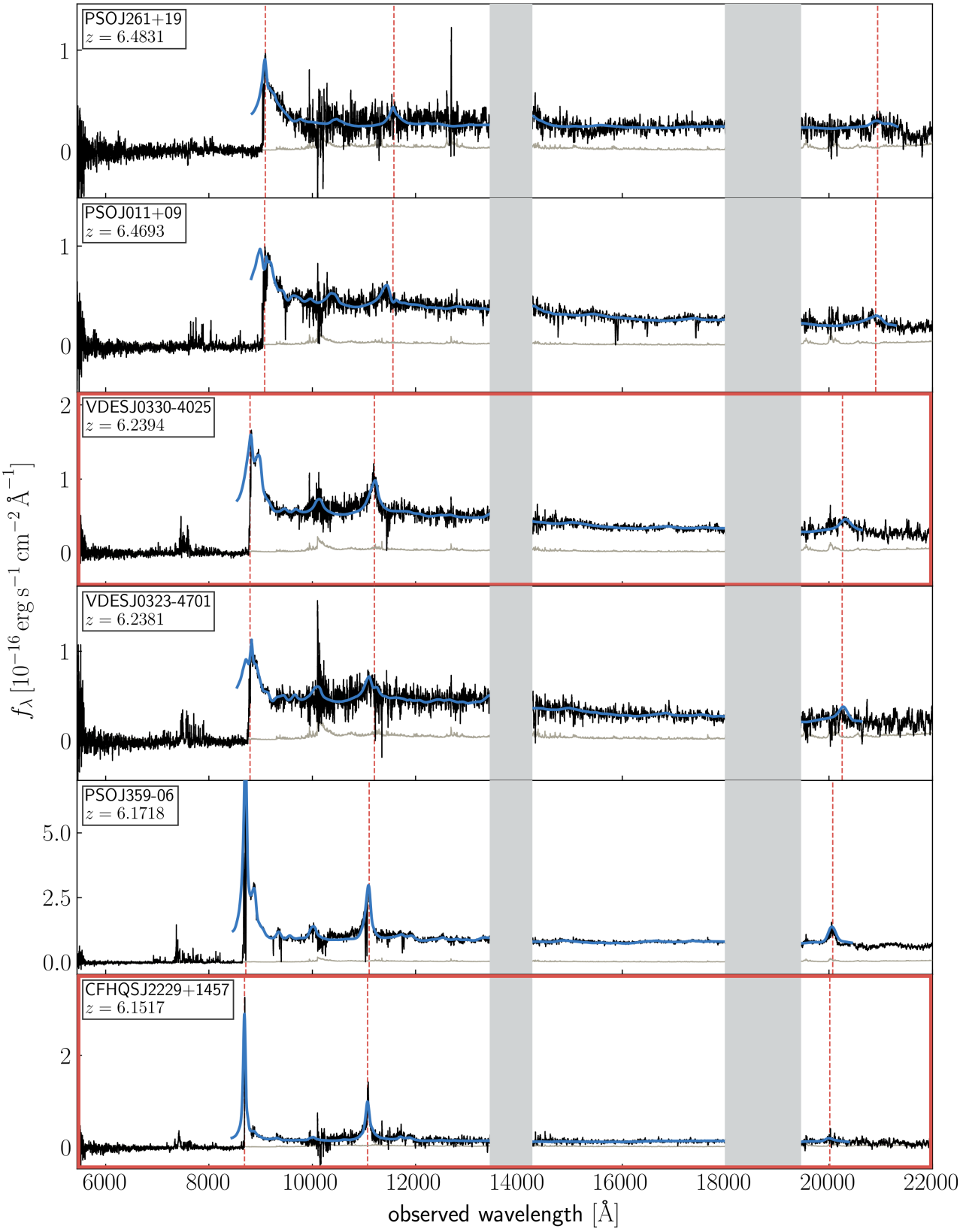


**Figure 10.** Same as Fig. 2 with quasar continuum estimates, shown in blue.

Di Matteo, T., Springel, V., & Hernquist, L. 2005, Nature, 433, 604

D'Odorico, V., Feruglio, C., Ferrara, A., et al. 2018, ApJL, 863, L29

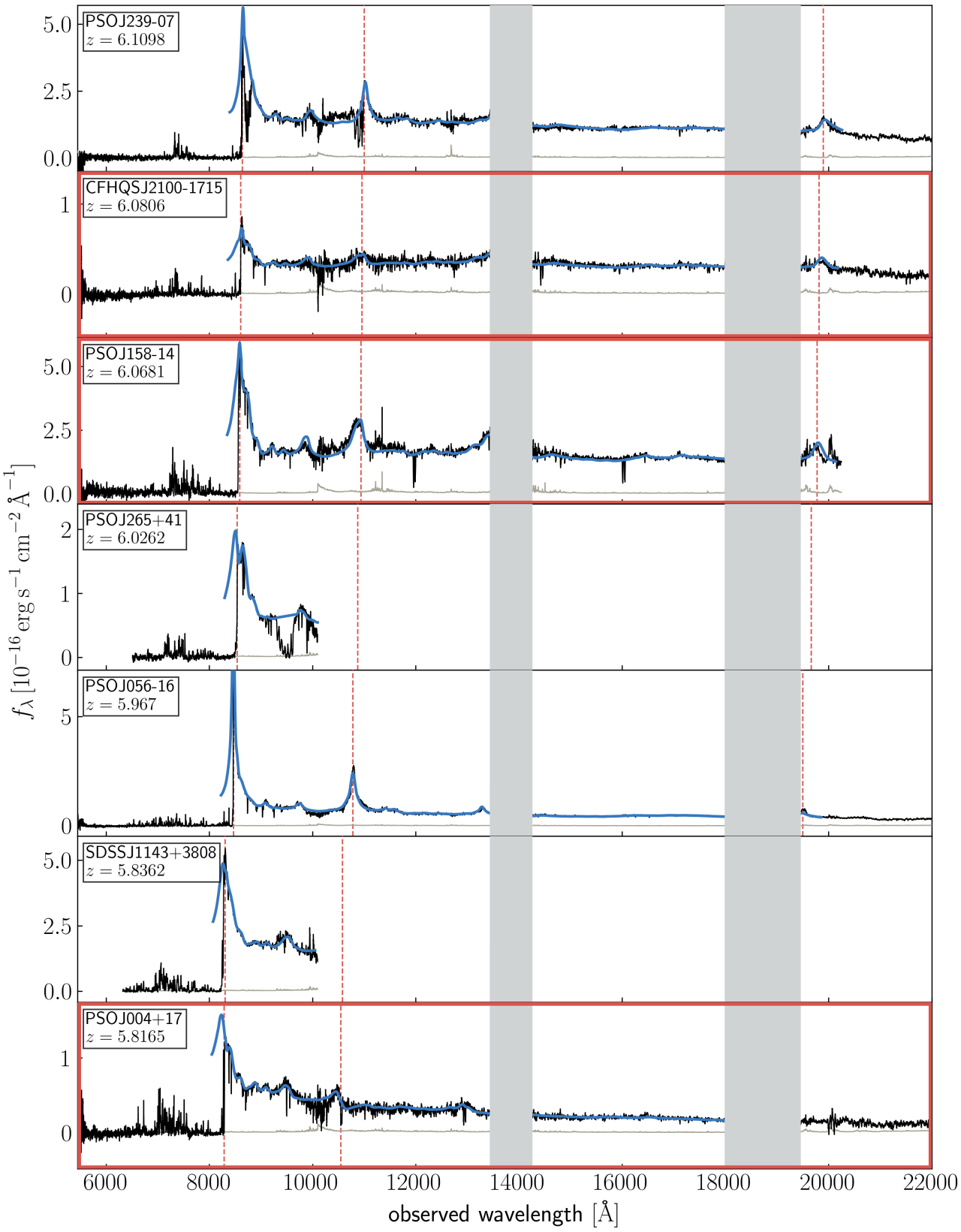


**Figure 11.** Same as Fig. 3 with quasar continuum estimates, shown in blue.

Dunne, L., Eales, S., Edmunds, M., et al. 2000, MNRAS, 315, 115

Eilers, A.-C., Davies, F. B., & Hennawi, J. F. 2018a, ApJ, 864, 53

Eilers, A.-C., Davies, F. B., Hennawi, J. F., & et al. in prep.
Eilers, A.-C., Davies, F. B., Hennawi, J. F., et al. 2017a, ApJ, 840, 24
Eilers, A.-C., Hennawi, J. F., & Davies, F. B. 2018b, ApJ, 867, 30
Eilers, A.-C., Hennawi, J. F., & Lee, K.-G. 2017b, ApJ, 844, 136
Fan, X., Strauss, M. A., Becker, R. H., et al. 2006, The Astronomical Journal, 132, 117
Farina, E. P., Arrigoni-Battaia, F., Costa, T., et al. 2019, ApJ, 887, 196
Foreman-Mackey, D., Hogg, D. W., Lang, D., & Goodman, J. 2013, Publications of the Astronomical Society of the Pacific, 125, 306
Gullikson, K., Dodson-Robinson, S., & Kraus, A. 2014, AJ, 148, 53
Habouzit, M., Volonteri, M., Latif, M., Dubois, Y., & Peirani, S. 2016, MNRAS, 463, 529
Haiman, Z., & Cen, R. 2001, in Astronomical Society of the Pacific Conference Series, Vol. 222, The Physics of Galaxy Formation, ed. M. Umemura & H. Susa, 101
Haiman, Z., & Hui, L. 2001, The Astrophysical Journal, 547, 27
Hennawi, J. F., Prochaska, J. X., Burles, S., et al. 2006, ApJ, 651, 61
Hopkins, P. F., Hernquist, L., Cox, T. J., et al. 2005, ApJ, 630, 716
Horne, K. 1986, PASP, 98, 609
Hunter, J. D. 2007, Computing In Science & Engineering, 9, 90
Inayoshi, K., Visbal, E., & Haiman, Z. 2019, arXiv e-prints, arXiv:1911.05791
Jiang, L., Fan, X., Vestergaard, M., et al. 2007, The Astronomical Journal, 134, 1150
Jones, E., Oliphant, T., Peterson, P., et al. 2001, SciPy: Open source scientific tools for Python, ,
Keating, L. C., Haehnelt, M. G., Cantalupo, S., & Puchwein, E. 2015, Monthly Notices of the Royal Astronomical Society, 454, 681
Kennicutt, R. C., & Evans, N. J. 2012, ARA&A, 50, 531
Khrykin, I. S., Hennawi, J. F., McQuinn, M., & Worseck, G. 2016, ApJ, 824, 133
Khrykin, I. S., Hennawi, J. F., & Worseck, G. 2019, MNRAS, 484, 3897
Lee, K.-G., Suzuki, N., & Spergel, D. N. 2012, AJ, 143, 51
Lidz, A., McQuinn, M., Zaldarriaga, M., Hernquist, L., & Dutta, S. 2007, ApJ, 670, 39
Lodato, G., & Natarajan, P. 2006, MNRAS, 371, 1813
Martini, P. 2004, Coevolution of Black Holes and Galaxies, 169
Martini, P., & Weinberg, D. H. 2001, The Astrophysical Journal, 547, 12
Mazzucchelli, C., Bañados, E., Venemans, B. P., et al. 2017, ApJ, 849, 91
McMullin, J. P., Waters, B., Schiebel, D., Young, W., & Golap, K. 2007, Astronomical Society of the Pacific Conference Series, Vol. 376, CASA Architecture and Applications, ed. R. A. Shaw, F. Hill, & D. J. Bell, 127
Mortlock, D. J., Warren, S. J., Venemans, B. P., et al. 2011, Nature, 474, 616
Novak, G. S., Ostriker, J. P., & Ciotti, L. 2011, ApJ, 737, 26
Onoue, M., Kashikawa, N., Matsuoka, Y., et al. 2019, ApJ, 880, 77
Pâris, I., Petitjean, P., Rollinde, E., et al. 2011, Astronomy & Astrophysics, 530, A50
Planck Collaboration, Ade, P. A. R., Aghanim, N., et al. 2014, A&A, 571, A1
Prochaska, J. X., Hennawi, J., Cooke, R., et al. 2019, PypeIt: Python spectroscopic data reduction pipeline, , , ascl:1911.004
Reed, S. L., McMahon, R. G., Martini, P., et al. 2017, MNRAS, 468, 4702
Reed, S. L., Banerji, M., Becker, G. D., et al. 2019, MNRAS, 487, 1874
Richards, G. T., Vanden Berk, D. E., Reichard, T. A., et al. 2002, The Astronomical Journal, 124, 1
Salpeter, E. E. 1964, The Astrophysical Journal, 140, 796
Schauer, A. T. P., Regan, J., Glover, S. C. O., & Klessen, R. S. 2017, MNRAS, 471, 4878
Schmidt, T. M., Worseck, G., Hennawi, J. F., Prochaska, J. X., & Crighton, N. H. M. 2017, ApJ, 847, 81
Shakura, N. I., & Sunyaev, R. A. 1973, A&A, 500, 33
Shen, Y., Strauss, M. A., Ross, N. P., et al. 2009, The Astrophysical Journal, 697, 1656
Shen, Y., Richards, G. T., Strauss, M. A., et al. 2011, ApJS, 194, 45
Soltan, A. 1982, MNRAS, 200, 115
Springel, V., White, S. D. M., Jenkins, A., et al. 2005, Nature, 435, 629
Suzuki, N., Tytler, D., Kirkman, D., O'Meara, J. M., & Lubin, D. 2005, ApJ, 618, 592
The Astropy Collaboration, Price-Whelan, A. M., Sipőcz, B. M., et al. 2018, ArXiv e-prints, arXiv:1801.02634
Trakhtenbrot, B., Volonteri, M., & Natarajan, P. 2017, ApJL, 836, L1
van der Walt, S., Colbert, S. C., & Varoquaux, G. 2011, Computing in Science Engineering, 13, 22
Venemans, B. P., Walter, F., Zschaechner, L., et al. 2016, ApJ, 816, 37

Venemans, B. P., McMahon, R. G., Walter, F., et al. 2012, ApJL, 751, L25
Venemans, B. P., Findlay, J. R., Sutherland, W. J., et al. 2013, The Astrophysical Journal, 779, 24
Venemans, B. P., Bañados, E., Decarli, R., et al. 2015, ApJL, 801, L11
Vestergaard, M., & Osmer, P. S. 2009, ApJ, 699, 800
Vestergaard, M., & Wilkes, B. J. 2001, ApJS, 134, 1
Visbal, E., Haiman, Z., & Bryan, G. L. 2014, MNRAS, 445, 1056
Volonteri, M. 2010, The Astronomy and Astrophysics Review, 18, 279
—. 2012, Science, 337, 544
Volonteri, M., Silk, J., & Dubus, G. 2015, ApJ, 804, 148
Walter, F., Riechers, D., Cox, P., et al. 2009, Nature, 457, 699
Wang, F., Wu, X.-B., Fan, X., et al. 2015, ApJL, 807, L9
Wang, F., Fan, X., Yang, J., et al. 2017, ApJ, 839, 27
Wang, F., Yang, J., Fan, X., et al. 2019, ApJ, 884, 30
White, M., Martini, P., & Cohn, J. D. 2008, MNRAS, 390, 1179
White, M., Myers, A. D., Ross, N. P., et al. 2012, MNRAS, 424, 933
Willott, C. J., Bergeron, J., & Omont, A. 2015, The Astrophysical Journal, 801, 123
Willott, C. J., Delorme, P., Omont, A., et al. 2007, The Astronomical Journal, 134, 2435
Willott, C. J., Delorme, P., Reylé, C., et al. 2009, The Astronomical Journal, 137, 3541
Willott, C. J., Albert, L., Arzoumanian, D., et al. 2010, The Astronomical Journal, 140, 546
Wu, X.-B., Wang, F., Fan, X., et al. 2015, Nature, 518, 512
Wyithe, J. S. B., Loeb, A., & Carilli, C. 2005, ApJ, 628, 575
Yang, J., Wang, F., Fan, X., et al. 2019a, AJ, 157, 236
Yang, J., Venemans, B., Wang, F., et al. 2019b, ApJ, 880, 153
Yu, Q., & Tremaine, S. 2002, MNRAS, 335, 965